



THE UNIVERSITY *of* EDINBURGH

Edinburgh Research Explorer

Osmotaxis in *Escherichia coli* through changes in motor speed

Citation for published version:

Rosko, J, Martinez, V, Poon, W & Pilizota, T 2017, 'Osmotaxis in *Escherichia coli* through changes in motor speed', *Proceedings of the National Academy of Sciences (PNAS)*, vol. 114, no. 38, pp. 7969-7976.
<https://doi.org/10.1073/pnas.1620945114>, <https://doi.org/10.1073/pnas.1620945114>

Digital Object Identifier (DOI):

[10.1073/pnas.1620945114](https://doi.org/10.1073/pnas.1620945114)
[10.1073/pnas.1620945114](https://doi.org/10.1073/pnas.1620945114)

Link:

[Link to publication record in Edinburgh Research Explorer](#)

Document Version:

Peer reviewed version

Published In:

Proceedings of the National Academy of Sciences (PNAS)

General rights

Copyright for the publications made accessible via the Edinburgh Research Explorer is retained by the author(s) and / or other copyright owners and it is a condition of accessing these publications that users recognise and abide by the legal requirements associated with these rights.

Take down policy

The University of Edinburgh has made every reasonable effort to ensure that Edinburgh Research Explorer content complies with UK legislation. If you believe that the public display of this file breaches copyright please contact openaccess@ed.ac.uk providing details, and we will remove access to the work immediately and investigate your claim.



Osmotaxis in *Escherichia coli* through changes in motor speed

Jerko Rosko^{*}, Vincent Martinez[†], Wilson Poon[†], Teuta Pilizota^{*}

^{*}Centre for Synthetic and Systems Biology, Institute of Cell Biology, School of Biological Sciences, University of Edinburgh, Alexander Crum Brown Road, EH9 3FF, Edinburgh, UK, and [†]Scottish Universities Physics Alliance and School of Physics & Astronomy, The University of Edinburgh, JCMB, Peter Guthrie Tait Road, Edinburgh EH9 3FD

Submitted to Proceedings of the National Academy of Sciences of the United States of America

Bacterial motility, and in particular repulsion or attraction towards specific chemicals, has been a subject of investigation for over 100 years, resulting in detailed understanding of bacterial chemotaxis and the corresponding sensory network in many bacterial species. For *Escherichia coli* most of the current understanding comes from the experiments with low levels of chemotactically-active ligands. However, chemotactically-inactive chemical species at concentrations found in the human gastrointestinal tract produce significant changes in *E. coli*'s osmotic pressure, and have been shown to lead to taxis. To understand how these nonspecific physical signals influence motility, we look at the response of individual bacterial flagellar motors under step-wise changes in external osmolarity. We combine these measurements with a population swimming assay under the same conditions. Unlike for chemotactic response, a long term increase in swimming/motor speeds is observed, and in the motor rotational bias, both of which scale with the osmotic shock magnitude. We discuss how the speed changes we observe can lead to steady state bacterial accumulation.

osmotaxis | bacterial flagellar motor | single motor experiments | bacterial taxis
| bacterial swimming

Abbreviations: BFM, bacterial flagellar motor; PMF, proton motive force; DDM, differential dynamic microscopy

Introduction

Many bacterial species are not only able to self propel (exhibit motility), but also direct their motion towards more favorable environments. This behavior, called taxis [1,2], has long been a subject of scientific investigation, as it serves a variety of purposes: seeking out nutrients and avoiding toxic substances [3,4], identifying thermal [5] and oxygen [6] gradients, as well as aiding pathogenic species in infecting their hosts [7,8]. The understanding of bacterial taxis is not only important when it comes to bacterial motility and accumulation; it also serves as a model for biological signal processing. Of particular interest are the precision [9,10], sensitivity [11] and robustness [12,13] that can be achieved with biological networks, and potentially utilized for human design purposes [14,15]. Specifically, bacterial chemotaxis, motion towards or away from specific chemicals [3], was first described over 120 years ago [16,17]. Since then, the systematic research efforts made it one of the best-studied topics in biology, especially when it comes to *Escherichia coli*.

E. coli swims by rotating a bundle of flagellar filaments [18,19], each powered by a bacterial flagellar motor (BFM), a rotary nano-machine that spins in the clockwise (CW) or counter-clockwise (CCW) direction [20]. Each bacterium possesses several individual motors randomly distributed along the cell body [19,21], which when rotating CCW enable formation of a stable filament bundle that propels the cell forward [22]. When one or, most likely, a few motors switch to CW rotation, their respective filaments fall out of the bundle, leading to a tumble event [19]. Forward swimming, likely in a different direction due to approximately random reorientation of the bacterial cell during the tumble event, resumes

when motors switch back to CCW direction and the bundle reforms [18,19].

The probability of **CW rotation** increases with the intracellular concentration of phosphorylated CheY protein (CheY-P) that interacts with the rotor of the BFM [23]. CheY-P is a part of a feedback control circuit, the chemotactic network [3], which relays outside information to the motor and allows *E. coli* to direct its motion. Inputs of the circuit are the methyl-accepting chemotactic proteins (MCPs), transmembrane proteins that bind specific ligands in the cell exterior [3], and through a signaling cascade affect the CheY-P to CheY ratio. When sensing attractants or repellents in nM to μ M range, the change in CheY-P to CheY ratio resets to the initial level within seconds, a characteristic feature of the network termed perfect adaptation [24]. Thus, directionality in the net motion of the cell arises through transient tuning of motor switching frequency in response to external stimuli [3].

The majority of work on *E. coli* chemotaxis over the last 40 years has been performed in a minimal phosphate buffer (termed Motility Buffer [25]). However, one of the primary habitats of *E. coli* is the gastrointestinal tract of humans and other warm-blooded animals [26,27]. This complex environment features not only various chemoattractants and repellents, but also spatial and temporal changes in osmolarity [28,30,31], which, in the stomach and intestine of humans, reach up to 500 mOsmol. The exact composition and osmolarity depend on the meal, ingestion history and location within the gastrointestinal tract [28,29].

Significance

Bacterial taxis has been a subject of active investigation for over 100 years, serving both as a model of biological sensory transduction and self-propulsion. Consequently, chemotaxis of *Escherichia coli* is one of the best understood biological networks. Nevertheless, the exact roles of taxis and motility in *E. coli*'s life cycle, particularly in host invasion, remain unknown, partly because of the complexity of its natural habitat. By looking at the response of both individual bacterial motors and a swimming population, we investigate *E. coli*'s response to changes in external osmolalities similar to those found in the human gastrointestinal tract. We find that, unlike chemotaxis, **osmotic response changes the motor speed and discuss how the observation can lead to previously observed osmotaxis.**

Reserved for Publication Footnotes

Sudden osmotic increases, termed hyperosmotic shocks or upshocks, cause cell volume shrinkage and require solute pumping and/or synthesis to re-inflate the cell and re-establish osmotic pressure [32,33]. Bacterial movement in search of environments with optimal water content, termed osmotaxis, has been discovered as early as 1889 [34]. Non-specific taxis away from sources of high concentrations has since been observed both in agar plate and capillary assays [35–38]. Yet, the behavior that leads to negative osmotaxis is less known [35,36,39,40], and contradictory observations have been reported. Osmotic stimuli can send a signal down the network through mechanical stimulation of chemoreceptors [41]; yet, free swimming cells were observed to tumble in response to an osmotic stimulus even when completely devoid of all components of the chemotactic network [35,40]. Intriguingly, this tumbling was later attributed to CCW rotation of flagella that normally results in cell runs [40]. The finding that osmotaxis on agar plates requires the presence of at least some chemosensors and all of the chemotactic signaling proteins further complicates the picture [35]. Open questions are thus left about the nature of this motile behavior that drives spatial accumulation, and its similarities, differences and possible interactions with taxis towards chemicals.

To clarify the exact nature of the osmotactic response, we study the phenomenon on both single cell and population levels, observing the rotation of individual flagellar motors under stepwise increases in osmolality, and measuring the swimming speeds of a population of ~ 10000 bacteria after exposure to an osmotic shock. The shock magnitudes we administer are motivated by those encountered in the human gastrointestinal tract [28,29]. We find that a stepwise increase in osmolality results in an elevated, long-term *CW Bias*. In addition, we observe osmokinetic post osmotic shock, i.e. significant changes in the motor, and consequently, swimming speeds of bacteria. Lastly, for higher shock magnitudes, we observe a loss of motor speed immediately post shock, followed by a speed recovery. We discuss how the observed non-adaptive response and osmokinetic can lead to taxis.

Results

Single motor response to an osmotic shock is complex. We begin with the reasonable assumption that at least one component of the chemotactic network responds to an osmotic stimulus in order to generate previously observed osmotactic behavior [35]. Then, the response should be evident in the output of the chemotactic network, the Clock-Wise (*CW*) bias of a single BFM. *CW bias* is defined as the fraction of time the BFM spends rotating in the clockwise direction [42]:

$$CW Bias = \frac{N_{cw}}{N_{tot}} \quad [1]$$

where N_{cw} is the number of data points corresponding to *CW* rotation and N_{tot} is the total number of data points in a given time interval.

To compute the *CW Bias*, we measured the speed of an individual BFM when exposed to a step-wise increase in the external osmolality. SI Appendix Fig. S1 gives a schematic of the bead assay used for measuring the motor speed [25,42]. Briefly, we attach cells to the cover slip and attach a latex bead, $0.5 \mu\text{m}$ in diameter, to a short filament stub [25,42]. The rotation of the BFM-driven bead is recorded using back-focal-plane interferometry at a 10 kHz sampling rate [43–45]. A representative single-motor rotation trace so obtained is shown in Fig. 1A. The shaded light blue interval shows the motor speed and rotational direction prior to osmotic stimu-

lus. Positive motor speed values represent CCW rotation and negative *CW*. Fig. 1B shows the histogram of the *CW Bias* obtained from the motor speed trace in A (*Methods*). Prior to the stimulus, the motor switches from CCW to *CW* rotation ~ 4 times per minute at *CW Bias* = 0.07, agreeing with previous studies [42,46].

At $t = 5\text{min}$, the extracellular osmolality is elevated by delivering 400 mM sucrose, at a flow rate of $\sim 120\mu\text{l}/\text{min}$ and local flow velocity $\sim 60\mu\text{m}/\text{sec}$ [47], causing an osmotic upshock of 488 mOsmol/kg. Immediately upon upshock, the motor stops switching rotational direction and speed drops. Then, a recovery phase begins (Fig. 1A and B, non-shaded time interval) with the motor speed gradually increasing while switching is absent. Post-recovery phase, which we define as the period after motor switching has resumed, is characterized by an increased switching frequency. Consequently, the *CW Bias* is also elevated (to 0.16), and is maintained over at least 20 min, suggesting that, unlike chemotaxis, the osmotactic response does not exhibit perfect adaptation [10,24]. The color map at the bottom of Fig. 1B is a compact representation of the histogram in Fig. 1B.

To determine if CheY-P is necessary for the osmotic response observed in Fig. 1A and B, we performed single-motor measurements on a strain lacking CheY (ΔCheY mutant [48,49]). A representative trace is shown in Fig. 1C, and several more traces are given in SI Appendix Fig. S2. The Recovery Phase of the ΔCheY mutant is the same as observed in Fig. 1A for the chemotactic wild type. However, the Post-recovery Phase of the mutant shows no switching events, indicating that CheY-P is necessary for the elevated bias observed in Fig. 1A and B.

Osmotic response does not exhibit perfect adaptation. We analyzed 69 cells exposed to three up-shock magnitudes to confirm the absence of perfect adaptation observed in Post-recovery Phase (Fig. 1A and B). Up-shocks were delivered as in Fig. 1, by exchanging VR Buffer (*Methods*) with the same buffer supplemented with 100, 200 and 400 mM sucrose, corresponding to osmotic shocks of 111, 230 and 488 mOsmol/kg (similar to osmolalities found in the human intestine [28,29], see also SI Appendix for osmolality measurements of all our buffers).

Fig. 2A shows color map histograms of each individual single-motor bias trace, where darker color represents higher *CW Bias* and white represents smooth swimming. The Recovery Phase, characterized by the zero *CW Bias* period, scales with the shock magnitude. SI Appendix Fig. S3 A shows the duration of the Recovery Phase, $T_{rec,CW}$, against the shock magnitude, where for the highest shock administered $T_{rec,CW} \sim 5\text{ min}$. The length of the Recovery Phase roughly corresponds to the time *E. coli* takes to recover its volume and osmotic pressure upon the hyperosmotic shock [50]. Throughout the Post-Recovery Phase, *CW Bias* levels do not, on average, relax to their initial pre-shock values. In our measurements this phase lasts for $\sim 10\text{-}20\text{ min}$, which is significantly longer than chemotactic adaptation times [10] even when saturating attractant concentrations are used [51].

Evidence for this assertion is shown in the *CW Bias* histograms in Fig. 2B, which shows a distribution computed from 3 min recordings in VR Buffer prior to shock, and Fig. 2C, which shows a distribution computed from 3 min intervals taken at various time points, 12 or more minutes after shock with 200 mM sucrose. Total of 120 single-motor recordings were used for the pre-shock condition and 96 for after. The median value of the population *CW Bias* shifts from 0.01 pre-shock to 0.06 after addition of 200 mM sucrose. Fig. 2D shows the median *CW Bias* in time for each of the three dif-

ferent shocks, calculated from the raw speeds of individual cells presented in Fig. 2A, using a 60 s wide moving window. Here, only medians are shown for clarity and the means, together with the interquartile range for each shock magnitude, are plotted in SI Appendix Fig. S3 B-D. While the *CW Bias* shows some recovery in time, in particular for 111 mOsmol/kg and 230 mOsmol/kg shocks, it proceeds on a slow time scale and the median values at the end of our measurement time remain elevated with respect to the initial value.

A further corroboration of long-term increase in *CW Bias* post osmotic shock comes from separating the *CW Bias* values of Fig. 2B according to the time point at which they were measured, relative to the administration of the osmotic shock ($t=0$). This is displayed in the inset of Fig. 2B and shows that the elevated *CW Bias* persists over a time scale as long as 1 h.

Osmotic response shows osmokinesis, i.e. changes in motor speed. The response to an osmotic upshock includes not only *CW Bias* dynamics, but also changes in motor and free-swimming speed. Fig. 3A shows a color map plot of normalized single-motor speeds of the same 69 cells presented in Fig. 2A. All cells were originally in VR Buffer and subsequently exposed to an osmotic upshock using 100, 200 or 400 mM sucrose, corresponding to upshifts of 111, 230 and 488 mOsmol/kg. BFM speeds were normalized with respect to the initial speed of each motor, i.e. to the average value of the first 15 seconds of the recording.

Following the osmotic upshock, motors show two kinds of behavior. If a shock is of a large magnitude, such as 488 mOsmol/kg, the speed drops sharply and significantly, with a period of speed recovery that follows. As can be seen from Fig. 3A and B the speed recovery ($T_{rec,\omega}$) lasts ~ 4.4 min on average (5.2 min median). This is of similar magnitude as $T_{rec,CW}$ (5.4 min mean, 5.0 min median, SI Appendix Fig. S4) and likely corresponds to the period of post-hyperosmotic shock volume recovery [50], however, $T_{rec,\omega}$ and $T_{rec,CW}$ for individual motors do not occur simultaneously (SI Appendix Fig. S4). After recovery, the speed increase continues, leading to elevated levels compared to the pre-shock values, Fig. 3C. Weaker upshocks, 111 and 230 mOsmol/kg, are characterized by an increase in motor speed without a significant speed drop, as seen in Fig. 3A-C. Elevated speed levels we observed are reversible. SI Appendix Fig. S5 shows motor speeds of cells exposed to 100 mM sucrose upshock, which have been allowed to recover prior to transferring them back to VRB. Upon recovery to the downshock motor speeds return to approximately the same initial levels.

To explore the population-level significance of our observation of osmokinesis in single cells, we next performed Differential Dynamic Microscopy (DDM) (see *Methods*) [52,53]. DDM is a fast, high-throughput method for measuring the distribution of swimming speeds in populations of a range of different self-propelled particles, averaging over up to $\sim 10^4$ particles at the same time. The technique is well suited for rapid scanning of parameter space, so that it also allowed us to extend the range of external osmolalities studied. DDM characterizes the motility of a population of particles (in our case *E. coli*) by analyzing the statistics of temporal fluctuations of pixel intensities in a sequence of low-optical resolution microscopy images, where the intensity fluctuations are caused by the variation in number density of particles. Specifically, we measure the differential image correlation function (DICF), which is effectively a power spectrum of the difference between two images taken at separate time points [52,53]. If a theoretical motility model exists, such as in the case of *E. coli* [22], the

expected DICF can be calculated and fitted to experimental data [53], allowing accurate estimates of the distribution of free-swimming speeds of a large number of bacteria [52].

Prior to DDM measurements cells were kept in VRB and osmotically shocked in a microfuge tube. Upon the upshock cells were quickly placed into a capillary for DDM measurements and the capillary was sealed, resulting in a fixed amount of oxygen present during the experiment. Swimming speed recordings commenced within 2 min after the upshock (*Methods*) and are shown in Fig. 3D. The gradual decrease of swimming speed with time observed in Fig. 3D for all magnitudes of osmotic upshocks was previously characterized in Motility Buffer, where *E. coli* maintains Proton Motive Force (PMF) using endogenous energy sources [54,55]. At fixed buffer composition, the time it takes to consume all available oxygen is inversely proportional to the cell concentration, and upon oxygen exhaustion a sudden ‘crash’ in swimming speed occurs [55]. Interestingly, we do not see such a ‘crash’ in swimming speed for the lowest five values of the imposed upshock, but do see a ‘crash’ when the upshock is at the highest value of 785 mOsmol/kg. Since the cell concentration is fixed, this implies that cells consume oxygen at a significantly higher rate at the highest osmotic shock.

The increase in BFM speed observed in single cells, Fig. 3A, translates to an increase in population swimming speed with increasing upshock magnitudes, Fig. 3D. Similarly, in agreement with Fig. 3A, for high shock magnitudes, in particular for 473 mOsm/kg and 785 mOsm/kg sucrose upshocks, a sharp speed drop is observed immediately upon upshock. We also see a period of speed recovery, with duration increasing with the shock magnitude.

In order to demonstrate that, on the time scales of our experiments, the speed increase is set by the external osmolality; in SI Appendix Fig. S7, as well as administering a sharp step increase, we upshocked the cells to VRB with 200 mM sucrose in a series of 10 steps, each 12 s apart, lasting 2 min in total. The DDM measurements commenced ~ 2 min after completion of the slower shock, and the slower shock shows identical speed behavior to that of the step increase.

Increasing sucrose concentrations results in the increased viscosity of the media, consequently increasing the drag coefficient on the motor (measured values of viscosity of our solutions are given in SI Appendix). In Fig. 3 we show BFM speeds and cell swimming speeds uncorrected for this effect, as the actual speed of the cell will be relevant for taxis. The viscosity corrected BFM speeds, calculated under the assumption that the motor torque does not change with the increasing viscosity, are shown in SI Appendix Fig. S8.

Furthermore, we check for the presence of steps during single motor speed recovery. To that end, in SI Appendix Fig. S9 we show examples of BFM speeds during the Recovery Phase after 488 mOsmol/kg upshock, starting just after the osmotic shock was administered. Majority of the traces do not show obvious steps during the BFM speed recovery period.

Discussion

Origins of osmotaxis. With no external stimuli *E. coli* swims in an almost straight line and re-orientes every so often in a nearly-random fashion, performing a random walk with an effective diffusion constant $D \sim v^2/\alpha$ [56,57], where v is the swimming speed and α the tumbling rate given by

$$\alpha = \frac{3(1 - \cos \phi_0)(\tau_{run} + \tau_t)}{\tau_{run}^2} \quad [2]$$

with τ_{run} , mean run time, $\phi_0 \sim 71^\circ$ mean reorientation angle following a tumble, and τ_t the duration of the tumble event [56, 58].

Upon sensing a sudden increase in attractant concentration, *E. coli* sharply elevates the CCW bias for ~ 1 s and then slightly lowers it for ~ 3 s, returning to the prestimulus level in ~ 4 s [24]. It is this characteristic impulse response of modulating the tumbling rate that allows *E. coli* to navigate towards a favorable environment. The detailed chemotactic performance and its origins have often been studied [56, 59–64].

The observation that a chemotactic mutant of *E. coli* (*CheR**CheB*) lacking normal methylation and demethylation enzymes does not show chemotactic accumulation, but does respond to raised attractant concentrations by lowering the tumble rate without adaptation [10, 24] lead researchers to calculate the consequences of spatially varying $\alpha(x)$ and $v(x)$ on steady state bacterial density [56, 63]. Similar calculations were performed for particles with v and α dependent on the local density [57], or when studying diffusion of bacteria in porous media [65]. These calculations offer possible explanations for previously observed negative osmotaxis, given the characteristic speed and bias response we here observed.

If we assume the simplest scenario, where there is no directional dependency of $\alpha(x)$ and $v(x)$; the steady state *E. coli* density will be inversely proportional to its swimming speed [57]:

$$\rho(x) \sim \frac{1}{v(x)} \quad [3]$$

In Fig. 3C we show motor speeds, ω , and in Fig. 4 mean CCW motor interval ($\bar{\tau}_{CCW}$) and tumbling rate (α) at a given osmolality. The ω and $\bar{\tau}_{CCW}$ were obtained from the last 3 min of the post-osmotic shock recordings presented in Fig. 3A, which represent the long term osmolality dependent changes. We then calculated α from $\bar{\tau}_{CCW}$ and $\bar{\tau}_{CW}$ (Fig. 4 and SI Appendix Fig. S10) using equation 2. The assumption was made that swimming speed v and the mean run time τ_{run} are proportional to the motor speed ω and the mean CCW interval $\bar{\tau}_{CCW}$, in agreement with previous studies [66], and our own DDM and motor measurements given in Fig. 3.

Thus, based on experimental results we present here and previous theoretical calculations (equation 3 [56, 57]) we would expect accumulation at lower osmolalities, equivalent to negative taxis previously observed [35]. The changes in tumbling rates suggest differences in the time dependent approach to steady state, but not the steady state density distribution itself [56, 63].

The theoretical calculations we refer to make the assumption that spatial gradients of $v(x)$ and $\alpha(x)$ are small [56, 57], such that we do not expect local gradients in steady state bacterial densities. For steeper osmotic gradients we expect a more complex osmotactic response, in particular since the Recovery Phases shown in Fig. 2 and Fig. 3 will no longer be vanishingly short, as we assumed above, which could explain some previous contradictory osmotactic observations [35, 40].

Our assumption that $\alpha(x)$ and $v(x)$ lack directional dependence in the case of osmotaxis, could be satisfied if the observed changes in α are not due to signaling within the chemotactic network, but purely due to changes in the interaction of CheY-P with the rotor units of the motor. For example, previous observations indicate that at higher external osmolalities, osmotic pressure is kept the same [50]. Thus, the crowding in an already crowded cytoplasm [67] increases, which can affect cytoplasmic interactions [68, 69] and the binding of CheY-P

to the BFM, perhaps in a similar fashion to that observed at higher hydrostatic pressures [70].

However, it is also possible that the observed changes in $\bar{\tau}_{CCW}$ and ω are a consequence of signal processing by the chemotactic network. In particular, Vaknin *et al.* reported that osmotically induced changes in cell volume can perturb the chemoreceptors, and that the signal could travel down some of the network components [41]. In such a scenario, $\alpha(x)$ and $v(x)$ would be directionally dependent (as in chemotactic response) and steady-state cell density would need to be calculated taking into account the directional dependency as well as the characteristic signal response we observed. Future work needs to investigate strains lacking specific parts of the network to determine the contribution of signaling and different components of the network to the osmotactic response.

Origins of osmokinesis. The large increase in motor speed post osmotic shock could be due to increases in PMF, possibly through alterations in cell metabolism; or, as an alternative explanation, due to the increase in number of stator units through mechanosensation [71, 72] or adaptive motor remodeling [12]. The BFM has been shown to act as a mechanosensor, increasing the number of stator units in response to higher loads [71, 72]. As the viscosity of the medium rises with addition of sucrose, the speed increase we observed could be due to the incorporation of additional stator units. In fact, at higher loads, an increase in the mean CW interval has been reported as well [71, 73]. At our load, a $0.5 \mu\text{m}$ bead attached to the motor via a short filament stub, the motor is still expected to operate in the high-load, ‘plateau’ region of the torque-speed curve [74, 75] with the estimated full number of stator units [75]. In addition, we observe an average **long term** 30 Hz increase in motor-speeds even at our lowest osmotic shocks where the viscosity of the solution hardly changes (it increases by 1.057 times). Furthermore, free-swimming cells with the motor operating in the linear-torque regime, where motor remodeling due to increased load is more likely, do not increase the swimming speed at viscosities well above the highest viscosity used in our experiments, as measured using Ficoll [83]. Therefore, it is less likely that additional stator unit incorporation or adaptive motor remodeling are sole explanations for the speed increases we observe.

SI Appendix Fig. S9 shows the motor speeds during the speed recovery phase for all of the BFMs recorded in the +488 mOsmol/kg condition. In majority of the traces no obvious steps are observed, suggesting that the increase in motor speed could be due to the increase in PMF with full set of stator units present. Here we note that the engagement of stator units with the rotor has been reported as torque dependent [72], where in absence of torque stator units disengage from the rotor. We would then expect stator resurrection during the Recovery Phase shown in SI Appendix Fig. S10. Absence of obvious step-wise increases indicates that volume shrinkage caused by the osmotic shock could affect motor dynamics and perhaps prevent, or slow down, stator disengagement.

The length of the motor speed recovery period observed in Fig. 3 is ~ 5 -10 min, in line with the volume recovery timescales observed previously post osmotic upshocks [33, 50]. The timescales of speed recovery (at similar shock magnitudes) observed from DDM data in Fig. 3D are longer, with recovery lasting ~ 40 min for the 473 mOsmol/kg upshock. Some variation in these times scales can be due to the difference between individual motor speed recovery and subsequent bundle formation. However, based on Fig. 3D, we suspect that greater contribution to the difference comes from alterations in oxygen consumption rate, which in turn shifts the time it takes

to reach the maximum swimming speeds.

By looking at individual BFMs and population swimming speeds together, we reveal the main characteristics of *E. coli*'s motility response to step increases in external osmolarity. The response consists of long term *CW Bias* and motor rotation/cell swimming speed increase. This is the first observa-

tion of osmokinesis in *E. coli*. We discuss how such observed speed increases can lead to negative taxis previously reported. Our study emphasizes the importance of investigating bacterial motility in environments that are closer to natural habitats, in the effort to understand the role and evolutionary advantage swimming offers to bacterial cells [76–78].

Fig. 1. (A) An example 30 min speed trace obtained from a single BFM. The cell was initially in VR Buffer (*Methods*), indicated in shaded light blue, and exposed to an osmotic upshock of 488 mOsmol/kg at $t=5$ min. The shock was delivered as a step increase by flowing in VRB containing additional 400 mM Sucrose, resulting in shock magnitude of 488 mOsmol/kg. (B) A histogram of clockwise bias computed by binning the trace in Fig. 1A into 30 second bins and dividing the time spent rotating clockwise by the bin length (see also equation 1 and *Methods*). Below is the same histogram condensed into a color map, with an intensity scale to the right. (C) Single-motor speed trace of a $\Delta CheY$ mutant exposed to the same osmotic upshock as in Fig. 1A.

Fig. 2. (A) Stacked single cell color maps (histograms) of *CW Bias* for three different shock magnitudes (indicated on the left). Bin widths are 30 s. VR Buffer was exchanged for the same buffer with the addition of sucrose at $t=5$ min. The white hatched column represents the period of the media exchanged whose duration was ~ 10 –15 s. 22, 24 and 23 cells are given for the 111, 230 and 488 mOsmol/kg condition, respectively. Color map scale is given at the top. (B) Histogram of *CW Bias* for cells prior to osmotic upshock (in VR Buffer) and (C) post osmotic upshock, administered by exchanging VRB with VRB + 200 mM sucrose. Bin width is set to 0.020. Total of 120 motors (each on a different cell) were used to construct Fig. 2B and 96 motors for Fig. 2C. Inset in Fig. 2C plots these 96 single motor biases against the time after their respective osmotic upshift. Gray shading represents the range between 25th and 75th percentile of the CW bias distribution in VR Buffer given in B. (D) Median population *CW Bias* in time, computed from cells given in Fig. 2A, for different shock magnitudes: 111 mOsmol/kg (red), 230 mOsmol/kg (green) and 488 mOsmol/kg (dark blue). Black arrow indicates the time at which hyperosmotic shock was administered.

Fig. 3. (A) Stacked single-motor (also single-cell) speed histograms, where the motor speed for each BFM is normalized to the average value of the first 15 s. Bin widths are 15 s and the color represents the bin height. Results are grouped by upshock magnitude, as indicated on the left hand edge. The white hatched column represents the point where an osmotic shock was performed by exchanging VR Buffer for VR Buffer + sucrose and the flow lasted for 10–15 s. 22, 24 and 23 cells are given for the 111, 230 and 488 mOsmol/kg conditions, respectively. The color map scale is given at the top of the figure. (B) Time necessary to recover the average value of pre-shock speed. Red horizontal bars are mean, and yellow triangles are median values, and the graph contains 18, 22, 23 and 20 single motor data points for the 0, 111, 230 and 488 mOsmol/kg upshocks. One value for the 230 mOsmol/kg condition and three for the 488 mOsmol/kg have been excluded from the graph as these motors do not recover average initial speed in the course of recording. The 0 mOsmol/kg condition is a buffer to buffer control flush, where we used the same shocking protocol as for osmotic upshocks. (C) Single motor speeds calculated as 3 min averages corresponding to a section between $t=17$ and $t=20$ min in A. The graph contains 12, 22, 24 and 23 single motor data points for the 0, 111, 230 and 488 mOsmol/kg upshocks. The 0 mOsmol/kg condition contains 12 out of 18 control flushes that were at least 20 min long. (D) DDM measurement of swimming speeds following an osmotic shock. Cells were shocked in microfuge tubes and brought into a microscope within 2 minutes. The legend shows shock magnitudes and the mean speed is the average of swimming speeds obtained for each time point in a range of different length scales (*Methods*). The systematic error of our measurements is then calculated as the standard deviation of the mean, and falls within $\sim 5\%$ of the mean value. Here it was not plotted for clarity.

Fig. 4. Mean counter clockwise motor interval, corresponding to cell runs, as a function of osmotic upshift. The “0” condition box contains 96 mean run intervals, calculated by averaging interval lengths over 5 min before osmotic upshift. Subsequent conditions, osmotic upshifts of 111, 230 and 488 mOsmol/kg, contain 21, 20 and 22 single-motor values calculated by averaging interval lengths over the time span from $t=12$ min to $t=15$ min after an osmotic shock. Not all cells were used to obtain $\bar{\tau}_{CCW}$ as note all cells had bound CCW intervals (see SI Appendix Fig. S11). In the inset, we calculate the tumbling rate α according to equation 2, approximating the run times with $\bar{\tau}_{CCW}$ and tumble times with $\bar{\tau}_{CW}$ given in SI Appendix Fig. S10.

Materials and Methods

E. coli strains and plasmids. E. coli strains KAF84 and KAF95 [49] were used for BFM speed and bias, and a highly motile MG1655 with an IS element inserted in the *flhD* operon regulatory region, which is the master operon for the expression of flagellar genes [79,80], for DDM experiments. Both KAF84 and KAF 95 carry the *flhC726* allele, (produce nonflagellate phenotypes), and contain a plasmid carrying an ampicillin resistance and a *flhC^{sticky}* gene (produces flagellar fillaments that stick readily to surfaces). Additionally, KAF84 is a chemotactic wild type and KAF95 is a Δ CheY strain and therefore can not perform chemotaxis, producing a smooth swimmer phenotype. MG1655 is a K-12 strain and a chemotactic wild type.

E. coli Growth and culturing. KAF95, KAF84 and MG1655 cells were grown in Tryptone Broth (1% Bacto tryptone, 0.5% NaCl) at 30°C while shaken at 200 RPM [42,52]. KAF95 and KAF84 were supplemented with 100 μ g/ml of ampicillin and grown to $OD_{600}=0.8-1.0$ (Spectronic 200E Spectrophotometer, Thermo Scientific, USA), and MG1655 to $OD_{600}=0.6$. We have calibrated the single scattering range of our spectrophotometer (SI Appendix Fig. S12) and ensured we stay within that range during OD_{600} readings by appropriately diluting the culture when needed [81]. In SI Appendix Fig. S12 we give the growth curves of the three strains we used for the experiments and indicate the OD_{600} at the point of culture harvest. After growth cells were washed into VR buffer (Volume Recovery) composed of the Modified Motility Buffer (MMB), which is 10 mM sodium phosphate buffer, pH=7.1 (an aqueous solution with 6.1mM of Na_2HPO_4 , 3.9 mM of NaH_2PO_4) and 0.01 mM of Ethylenediaminetetraacetic acid (EDTA), with added Glycine Betaine, Potassium Chloride and Choline Chloride to final concentrations of 10, 20 and 10 mM, respectively. These compounds act as osmoprotectants and allow the cell to recover volume after an osmotic shock. MMB is a variant of the Motility Buffer, commonly used in flagellar motor and chemotaxis experiments [25,42], with sodium phosphates substituted for potassium phosphates. After washing, all the experiments were performed in VR buffer. KAF95 and KAF84 cells were washed by centrifuging them into a pellet and exchanging solution, while MG1655 cells were washed by gentle filtration to preserve filaments [55] and experiments were performed in VR buffer as for motor speed measurements.

Sample preparation and osmotic shock. For BFM experiments flagellar filaments were truncated by passing a bacterial suspension through two syringes with narrow gauge needles (26G) connected with a plastic tube (‘shearing device’ [25,42,82]). Subsequently, cells with truncated filaments were washed by centrifugation. Slides for BFM experiments were prepared as before [42,82] by layering two parallel strips of double sided sticky tape onto a microscope slide and covering them with a cover glass, forming a tunnel slide (SI Appendix Fig. S1) of approximate volume of $\sim 8 \mu$ l. 1% poly-L-lysine was loaded into the tunnel and extensively washed out after keeping it in for ~ 10 s to allow glass coating. Cells with truncated filaments were loaded into the tunnel and incubated for 10 min in a humid environment to prevent evaporation. Subsequently, non attached cells were washed out. Next, 0.5 μ m beads in diameter (Polysciences) were added and incubated for 10 min to allow sticking to the filaments and excess beads were washed out post incubation. Osmotic shocks were performed while the slide was in the microscope by adding 24 μ l of the shocking solution to one end and immediately bringing a piece of tissue paper to the other, resulting in flow

and exchange of media. The flow duration was approximately 10-15 s and the local flow velocity next to the attached bacterium was 60 μ m/sec [47]. Tunnel was sealed after the shock to prevent evaporation and thus potential further increase in osmolality throughout the course of the experiment. For DDM experiments an $\sim 400 \mu$ m deep flat capillary (Vitrocom) glass sample was filled with $\sim 150 \mu$ l of bacterial suspension immediately after upshock, and subsequently sealed to prevent evaporation during the experiment. Osmolalities of the solutions were measured with a freezing point depression osmometer (Camlab) and are listed in SI.

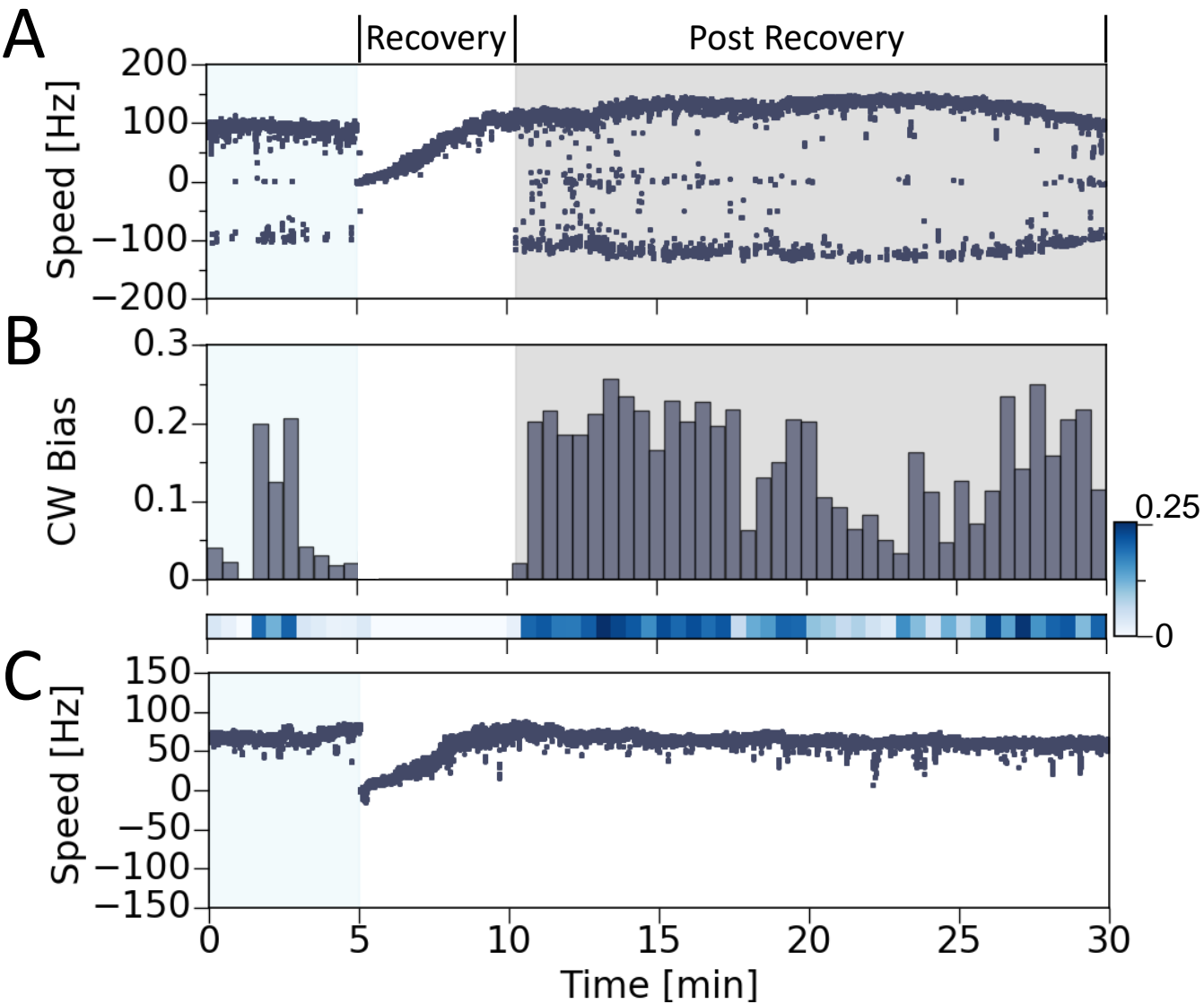
Microscopy and data collection. For BFM experiments backfocal plane interferometry [43,44] was performed using a custom built microscope and an 855 nm laser (Blue Sky Research, USA) which formed a weak optical trap. The rotating bead attached to a flagellar stub was brought into the focus of the laser and the back-focal plane of the condenser was imaged onto a position sensitive detector (PSD Model 2931, New Focus, USA). The voltage signal from the PSD was passed through an analog anti-aliasing filter (low pass, Bessel type filter with a cut off frequency of 2.5 kHz, Krohn-Hite Corporation, USA) and sampled at 10 kHz (PCIE-6351 DAQ, National Instruments). For DDM experiments imaging within the glass capillary was performed at 100 μ m away from the bottom of the capillary to avoid any interaction with the glass wall. The imaging begun within ~ 2 min post upshock, and consisted of a time-series of phase-contrast images (Nikon TE300 Eclipse fitted with a Nikon Plan Fluor 10Ph1 objective, NA=0.3, Ph1 phase-contrast illumination plate). Imaging was performed at 100 Hz sampling rate (Mikrotron high-speed camera (MC 1362) and frame grabber (Inspecta 5, 1-Gb memory)) for ~ 40 s per movie duration and using 512x512 pixels field of view. Both DDM and BFM experiments were performed at room temperature ($21 \pm 1^\circ$ C).

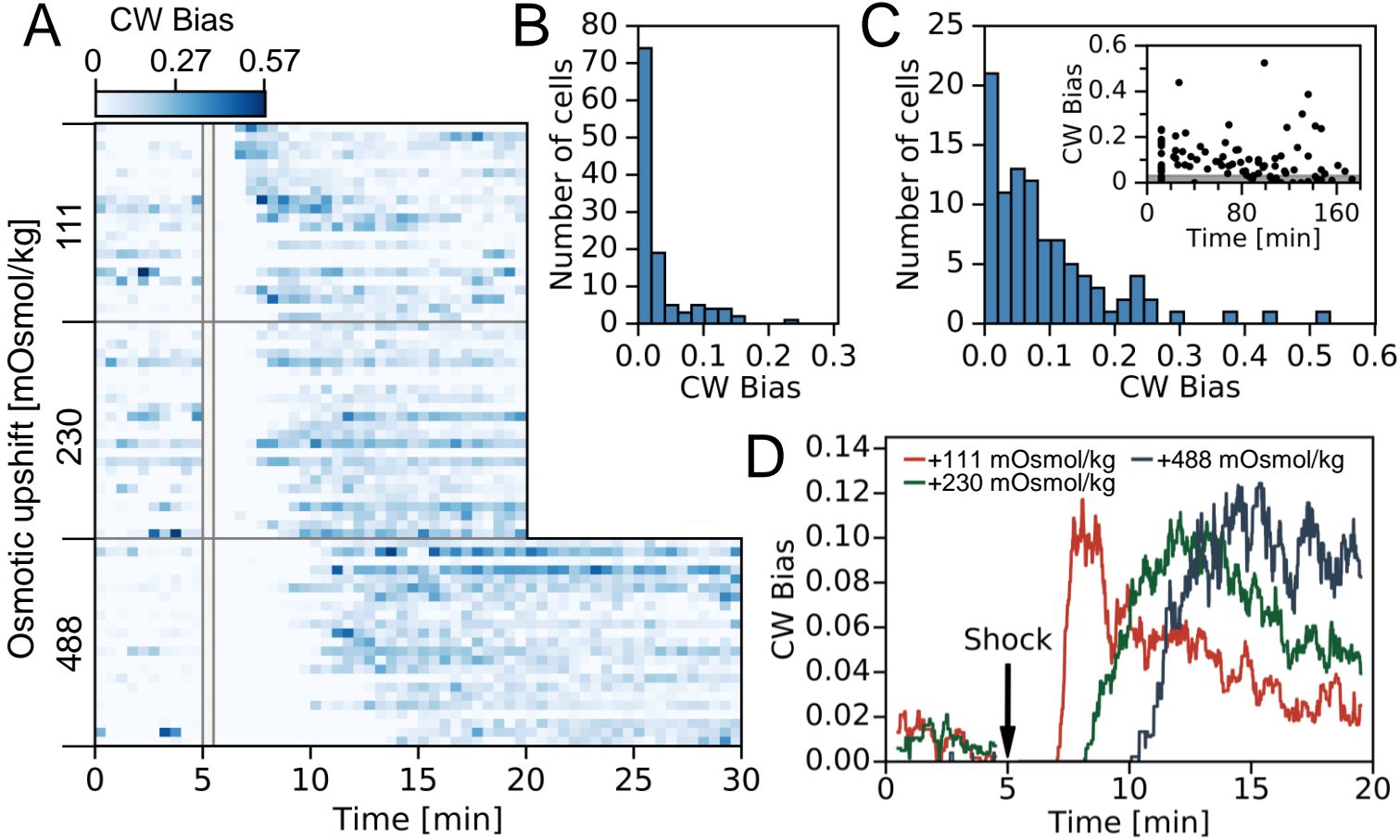
Data analysis. Data collected during BFM experiments was analyzed in the following way. X and Y signals (obtained from voltages from the PSD) were passed through a moving window discrete Fourier transform, where the window moves point by point and the window size was 1.684 s. Time traces of single motor speed obtained in such a way were processed to calculate the CW Bias using Equation 1. CW Biases were calculated for fixed interval sizes (30 s in Fig. 2A, 3 min in Fig. 2C and 5 min in Fig.2B), and using a 60 s long moving window in Fig. 2D and SI Appendix Fig. S3B-E. To calculate $\bar{\tau}_{CCW}$ we first take a mean of the τ_{CCW} intervals belonging to each individual BFM rotation trace. We then pool so obtained mean cell intervals into a distribution and obtain its mean (similar is true for $\bar{\tau}_{CW}$, but in opposite direction). We include only bound CCW and CW intervals (see Fig. S7). In DDM experiments, the mean swimming speed was calculated from DDM movies as an average over $\sim 10^4$ cells/ml. Details of the image processing and data analysis were as before [52,53,55,83]. DDM allows the measurement of an advective speed, simultaneously, over a range of spatial-frequency q , where each q defines a length-scale $L=2\pi/q$ (for more details, see [52,53]). A mean swimming speed is extracted by averaging over q . Data plotted in Fig. 3D were obtained by averaging over the range $0.5 \lesssim q \lesssim 2.2 \mu\text{m}^{-1}$, corresponding to a range in length-scale $3 \lesssim L \lesssim 13 \mu\text{m}$.

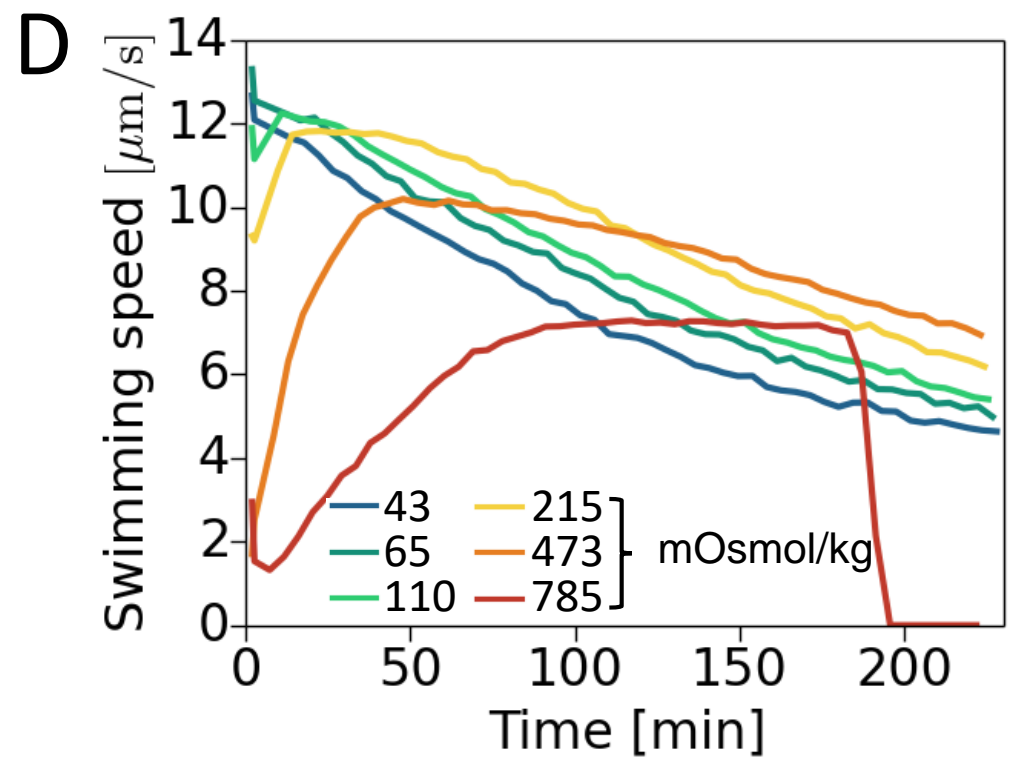
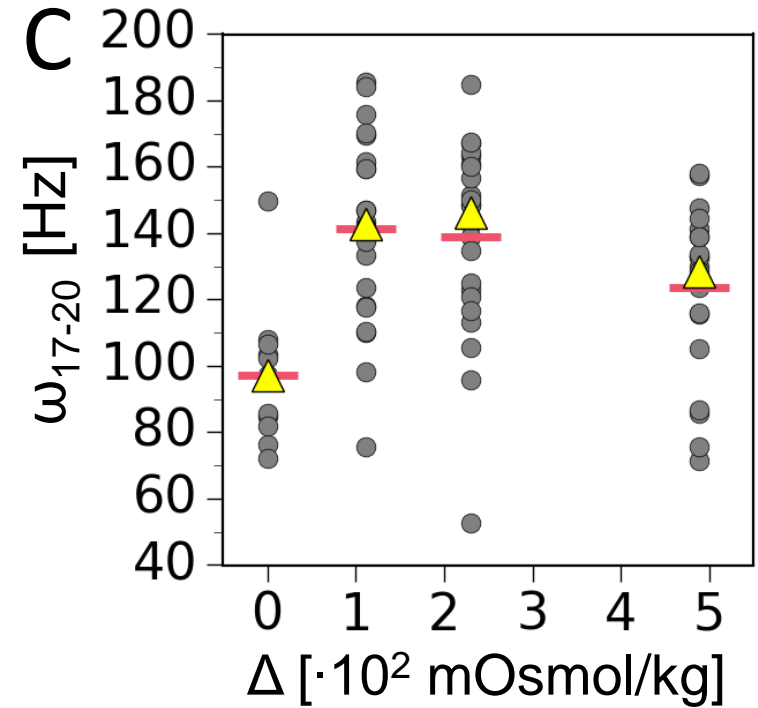
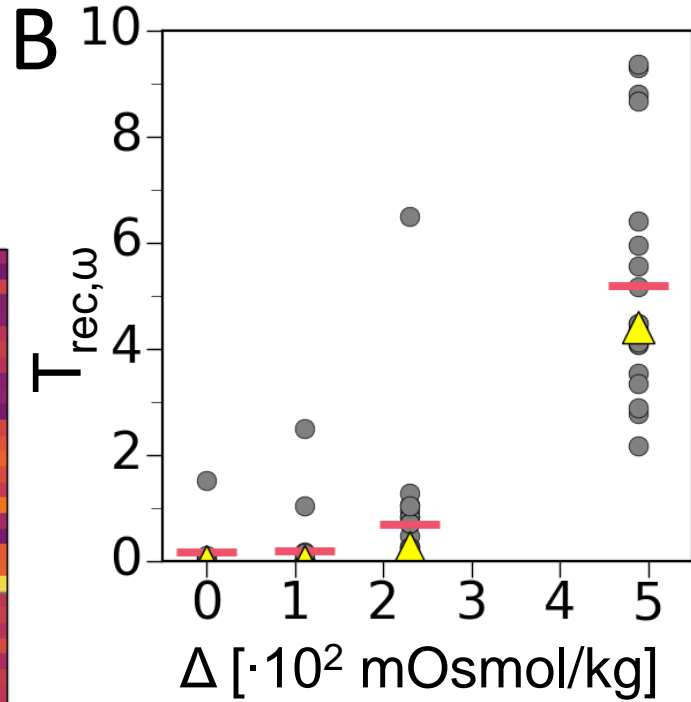
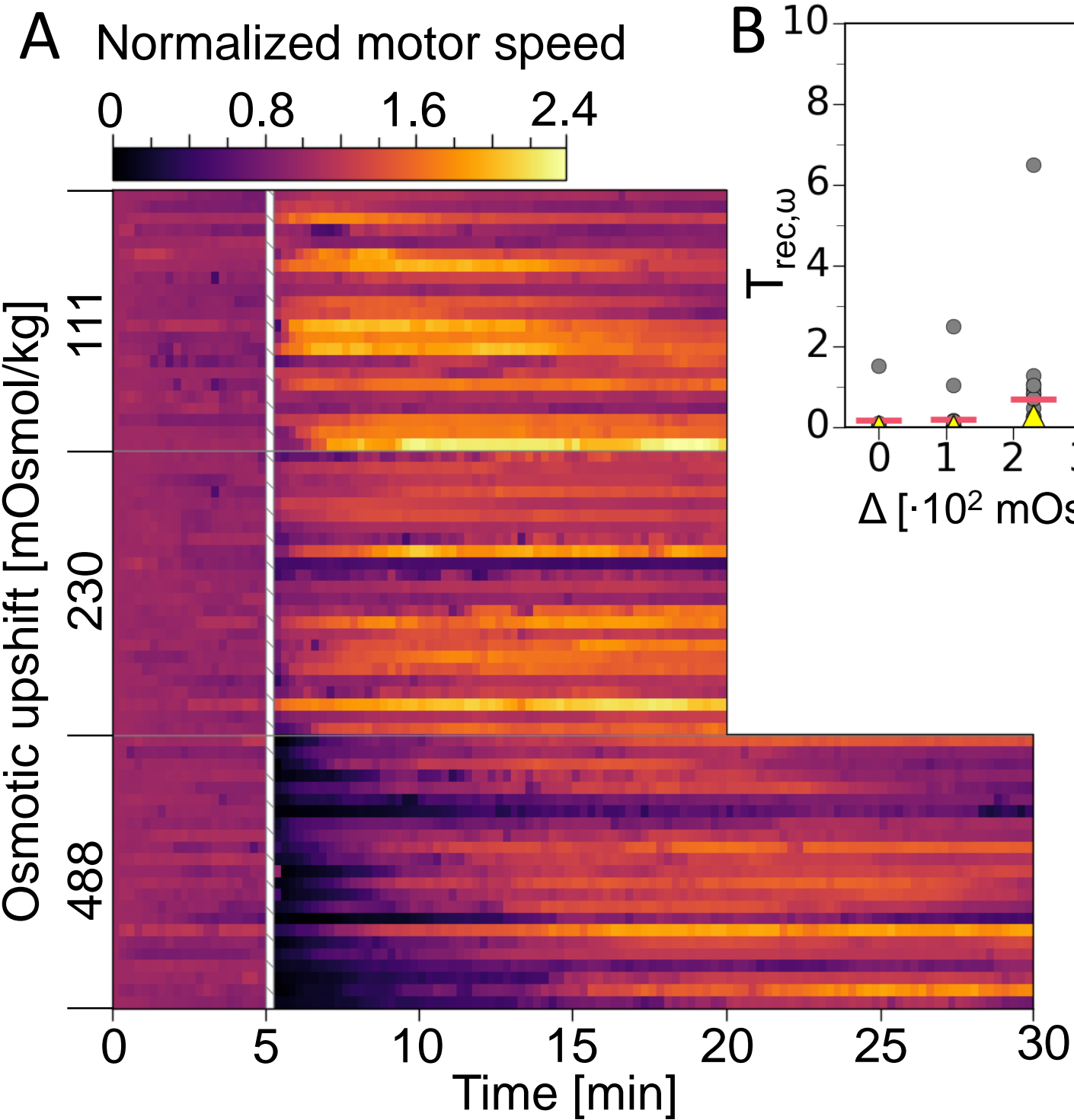
ACKNOWLEDGMENTS. This work was supported by Chancellor’s Fellowship to TP. WCKP and VM were funded by an EPSRC Programme Grant EP/J007404/1 and an ERC advanced grant (AdG 340877 PHYSAPS). We thank all of the members of the Pilizota lab, Jana Schwarz-Linek, Alex Morozov and Filippo Menolascina for useful discussions and support.

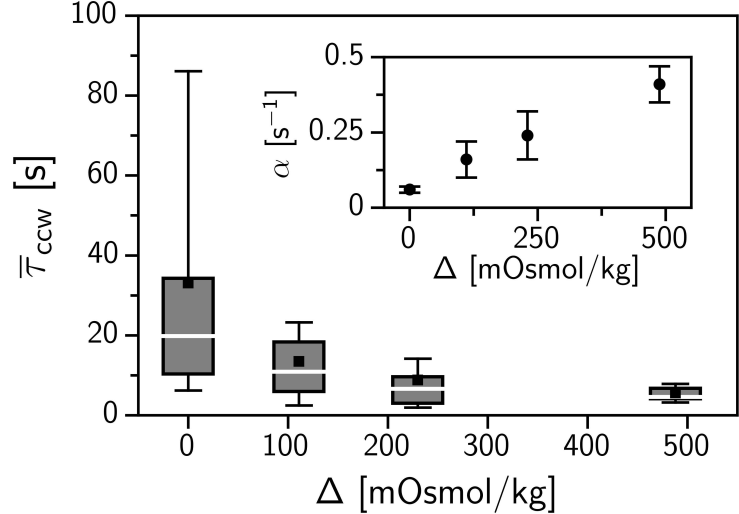
1. Krell T, Laca J, Muoz-Martinez F, Reyes-Darias JA, Cadirci BH, Garca-Fontana C, Ramos JL. (2011) Diversity at its best: bacterial taxis.
2. Purcell, EM. (1977) Life at low Reynolds number. *American Journal of Physics* 45:3-11
3. Wadhams GH, Armitage JP (2004) Making sense of it all: bacterial chemotaxis. *Nat Rev Mol Cell Biol* 5(12):1024-1037.
4. Adler J (1969) Chemoreceptors in bacteria. *Science* 166(3913):1588-1597
5. Paster E, Ryu WS (2007) The thermal impulse response of *Escherichia Coli*. *Proc Natl Acad Sci USA* 105(14):5373-5377.
6. Adler M, Erickstad M, Gutierrez E, Groisman A (2012) Studies of bacterial aerotaxis in a microfluidic device. *Lab Chip* 12(22): 4835-4847
7. Rivera-Chvez F, Winter SE, Lopez CA, Xavier MN, Winter MG, Nuccio SP, Russell JM, Laughlin RC, Lawhon SD, Sterzenbach T, Bevins CL, Tsois RM, Harshey R, Adams LG, Bumler AJ. *Salmonella Uses Energy Taxis to Benefit from Intestinal Inflammation*. *PLOS Pathog* 9(4):e1003267 (2013).
8. Cullender TC, Chassaing B, Janzon A, Kumar K, Muller CE, Werner JJ, Angenent LT, Bell ME, Hay AG, Peterson DA, Walter J, Vijay-Kumar M, Gewirtz AT, Ley RE. (2013) Innate and adaptive immunity interact to quench microbiome flagellar motility in the gut. *Cell Host Microbe* 14(15):571-581
9. Neumann S, Vladimirov N, Krembel AK, Wingreen NS, Sourjik V (2014) Imprecision of Adaptation in *Escherichia coli* Chemotaxis. *PLoS ONE* 9(1): e84904. doi:10.1371/journal.pone.0084904
10. Segal JE, Block SM, Berg HC (1986) Temporal comparisons in bacterial chemotaxis. *Proc Natl Acad Sci USA* 83(23):8987-8991
11. Cluzel P, Surette M, Leibler S (2000) An ultrasensitive bacterial motor revealed by monitoring signaling proteins in single cells. *Science* 287(5458):1652-1655
12. Yuan J, Branch RW, Hosu BG, Berg HC (2012) Adaptation at the output of the chemotaxis signalling pathway. *Nature* 484(7393):233-236
13. Lele PP, Branch RW, Nathan VS, Berg HC (2012) Mechanism for adaptive remodeling of the bacterial flagellar switch. *Proc Natl Acad Sci USA* 109(49):20018-20022
14. Navlakha S, Bar-Joseph Z (2014) Algorithms in nature: the convergence of systems biology and computational thinking. *Mol Syst Biol*. 7:546-546
15. Babaoglu O, Canright G, Deutsch A, Di Caro GA, Ducatelle F, Gambardella LM, Ganguly N, Jelasky M, Montemanni R, Montresor A, Urnes T (2006) Design Patterns from Biology for Distributed Computing. *ACM Trans. Auton. Adapt. Syst.* 1:26-66
16. Pfeffer W (1884) Locomotorische Richtungsbewegungen durch chemische Reize. *Unters. Bot. Inst. Tübingen* 1:363-482
17. Pfeffer W (1888) X. *Unters. Bot. Inst. Tübingen* 2:582-Y
18. Berg HC, Anderson RA (1973) Bacteria Swim by Rotating their Flagellar Filaments. *Nature* 245:380-382.
19. Turner L, Ryu WS, Berg HC (2000) Real-Time Imaging of Fluorescent Flagellar Filaments. *Journal of Bacteriology* 182(10):2793-2801
20. Sowa Y, Berry RM (2008) Bacterial flagellar motor. *Quarterly Reviews of Biophysics* 41(02):103-132.
21. Tang H, Blair DF (1995) Regulated underexpression of the Flm protein of *Escherichia coli* and evidence for a location in the flagellar motor distinct from the MotA/MotB torque generators. *J Bacteriol.* 177(12):3485-3495
22. Berg HC (2003) The Rotary Motor of Bacterial Flagella. *Annual Review of Biochemistry* 72:19-54
23. Welch M, Oosawa K, Aizawa S, Eisenbach M (1993) Phosphorylation-dependent binding of a signal molecule to the flagellar switch of bacteria. *Proc Natl Acad Sci USA* 90(19):8787-8791
24. Block SM, Segall JE, Berg HC (1982) Impulse responses in bacterial chemotaxis. *Cell* 31(1):215-226
25. Ryu WS, Berry RM, Berg HC. (2000) Torque-generating units of the flagellar motor of *Escherichia coli* have a high duty ratio. *Nature* 403(6768):444-447
26. Berg RD (1996) The indigenous gastrointestinal microflora. *Trends Microbiol* 4(11):430-435
27. Gordon DM, Cowling A (2003) The distribution and genetic structure of *Escherichia coli* in Australian vertebrates: host and geographic effects. *Microbiology* 149:3575-3586
28. Fordtran JS, Locklear TW (1966) Ionic constituents and osmolality of gastric and small-intestinal fluids after eating. *Am J Dig Dis.* 11(7):503-521
29. Reppas C, Karatza E, Goumas C, Markopoulos C, Vertzoni M (2015) Characterization of Contents of Distal Ileum and Cecum to Which Drugs/Drug Products are Exposed During Bioavailability/Bioequivalence Studies in Healthy Adults. *Pharm Res* 32:3338-3349.
30. Datta SS, Preska Steinberg A, Ismagilov RF (2016) Polymers in the gut compress the colonic mucus hydrogel. *Proc Natl Acad Sci USA.* 113(26):7041-7046.
31. Begley M, Gahan CGM, Hill C (2015) The interaction between bacteria and bile. *FEMS Microbiol Rev* 29(4):625-651
32. Wood JM (2015) Bacterial responses to osmotic challenges. *J Gen Physiol* 145(5):381-388
33. Pilizota T, Shaevit JW (2012) Fast, multiphase volume adaptation to hyperosmotic shock by *Escherichia coli*. *PLoS One* 7(4):e35205.
34. Massart J (1889) Sensibilit et adaptation des organismes la concentration de solutions salines. *Arch. Biol.* 9:515-570
35. Li C, Boileau AJ, Kung C, Adler J (1988) Osmotaxis in *Escherichia coli*. *Proc. Natl. Acad. Sci. U.S.A.* 85(24):9451-9455
36. Adler J, Li C, Boileau AJ, Qi Y, Kung C (1988) Osmotaxis in *Escherichia coli*. *Cold Spring Harb. Symp. Quant. Biol.* 53:19-22
37. Oosawa K, Imae Y (1983) Glycerol and ethylene glycol: members of a new class of repellents of *Escherichia coli* chemotaxis. *J. Bacteriol.* 154(1):104-112
38. Tso WW, Adler J (1974) Negative Chemotaxis in *Escherichia coli*. *J. Bacteriol.* 118(2):560-576
39. Berg HC (1974) Dynamic properties of bacterial flagellar motors. *Nature.* 249:77-79
40. Li C, Adler J (1993) *Escherichia coli* shows two types of behavioral responses to osmotic upshift. *J Bacteriol* 175(9): 2564-2567
41. Vaknin A, Berg HC (2006) Osmotic stress mechanically perturbs chemoreceptors in *Escherichia coli*. *Proc Natl Acad Sci USA* 103(3):592-596
42. Bai F, Branch RW, Nicolau DV Jr, Pilizota T, Steel BC, Maini PK, Berry RM (2010) Conformational Spread as a Mechanism for Cooperativity in the Bacterial Flagellar Switch. *Science* 327(5966):685-689
43. Denk W, Webb WW (1990) Optical measurement of picometer displacements of transparent microscopic objects. *Appl Opt.* 29(16):2382-2891
44. Svoboda K, Schmidt CF, Schnapp BJ, Block SM (1993) Direct observation of kinesin stepping by optical trapping interferometry. *Nature* 365(6448):721-727
45. Pilizota T, Bilyard T, Bai F, Futai M, Hosokawa H, Berry RM (2007) A Programmable Optical Angle Clamp for Rotary Molecular Motors. *Biophys J.* 93(1): 264-275
46. Bai F, Che YS, Kami-ike N, Ma Q, Minamino T, Sowa Y, Namba K (2013) Populational Heterogeneity vs. Temporal Fluctuation in *Escherichia coli* Flagellar Motor Switching. *Biophys. J.* 105(9):2123-2129
47. Buda R, Liu Y, Yang J, Hegde S, Stevenson K, Bai F and Pilizota T (2016) Dynamics of *Escherichia coli*'s passive response to a sudden decreases in external osmolality. *Proc Natl Acad Sci USA.* September 2016, doi:10.1073/pnas.1522185113
48. Fahrner KA (1995) Studies of bacterial flagellar motors and filaments. Ph.D. thesis. Harvard University, Cambridge, MA
49. Berg HC, Turner L (1993) Torque generated by the flagellar motor of *Escherichia coli*. *Biophys J* 65(5):2201-2216
50. Pilizota T, Shaevit JW (2014) Origins of *Escherichia coli* growth rate and cell shape changes at high external osmolality. *Biophys J.* 107(8):1962-1969
51. Berg HC, Tedesco PM (1975) Transient response to chemotactic stimuli in *Escherichia coli*. *Proc Natl Acad Sci USA* 72(8):3235-3239
52. Martinez VA, Besseling R, Croze OA, Tailleux J, Reuter M, Schwarz-Linek J, Wilson LG, Bees MA, Poon WC (2012) Differential Dynamic Microscopy: A High-Throughput Method for Characterizing the Motility of Microorganisms. *Biophys J.* 103(8):1637-1647
53. Differential dynamic microscopy of bacterial motility. Wilson LG, Martinez VA, Schwarz-Linek J, Tailleux J, Bryant G, Pusey PN, Poon WC. (2011) Differential Dynamic Microscopy of Bacterial Motility. *Phys. Rev. Lett.* 106(1):018101
54. Dawes E, Ribbons D (1965) Studies on the Endogenous Metabolism of *Escherichia Coli*. *Biochem J.* 95:332
55. Schwarz-Linek J, Arlt J, Jepson A, Dawson A, Vissers T, Miroli D, Pilizota T, Martinez VA, Poon WC. (2016) *Escherichia coli* as a model active colloid: A practical introduction. *Colloids Surf B Biointerfaces* 137:2-16
56. Schnitzer MJ (1993) Theory of continuum random walks and application to chemotaxis. *Phys Rev E.* 48(4):2553-2568
57. Tailleux J, Cates ME (2008) Statistical Mechanics of Interacting Run-and-Tumble Bacteria. *Phys Rev Lett.* 100(21):218103
58. Lovely PS, Dahlquist FW (1975) Statistical measures of bacterial motility and chemotaxis. *J Theor Biol.* 50(2):477-496
59. Clark DA, Grant LC (2005) The bacterial chemotactic response reflects a compromise between transient and steady-state behavior. *Proc Natl Acad Sci USA.* 102(26): 9150-9155
60. de Gennes PG (2004) Chemotaxis: the role of internal delays. *Eur Biophys J.* 33(8): 691-693
61. Strong SP, Freedman B, Bialek W, Koberle R (1998) Adaptation and optimal chemotactic strategy for *E. coli*. *Phys Rev E* 57(4):4604-4617
62. Cates ME (2012) Diffusive transport without detailed balance in motile bacteria: does microbiology need statistical physics? *Rep Prog Phys.* 75(4):042601
63. Schnitzer MJ, Block SM, Berg HC, Purcell EM (1990) Strategies for Chemotaxis. *Symp Soc Gen Microbiol* 46: 15-33
64. Celani A, Vergassola M (2010) Bacterial strategies for chemotaxis response. *Proc Natl Acad Sci USA.* 107(4):1391-1396
65. Licata NA, Mohari B, Fuqua C, Setayeshgar S (2016) Diffusion of Bacterial Cells in Porous Media. *Biophys. J.* 110(1):247-257
66. Magariyama Y, Sugiyama s, Muramoto K, Kawagishi I, Imae Y, Kudo s (1995) Simultaneous measurement of bacterial flagellar rotation rate and swimming speed. *Biophys. J.* 69(5):2154-2162
67. Parry BR, Surovtsev IV, Cabeen MT, O'Hern CS, Dufresne ER, Jacobs-Wagner C (2014) The bacterial cytoplasm has glass-like properties and is fluidized by metabolic activity. *Cell* 156(1-2):183-194
68. Klumpp S, Scott M, Pedersen S, Hwa T (2013) Molecular crowding limits translation and cell growth. *Proc Natl Acad Sci USA* 110(42):16754-16759
69. Paudel BP, Rueda D (2014) Molecular Crowding Accelerates Ribozyme Docking and Catalysis. *J Am Chem Soc.* 136(48):16700-16703
70. Nishiyama M, Sowa Y, Kimura Y, Homma M, Ishijima A, Terazima M. (2013) High Hydrostatic Pressure Induces Counterclockwise to Clockwise Reversals of the *Escherichia coli* Flagellar Motor. *J Bacteriol.* 195(8):1809-1814
71. Lele PP, Hosu BG, Berg HC (2013) Dynamics of mechanosensing in the bacterial flagellar motor. *Proc Natl Acad Sci USA.* 110(29):11839-44
72. Tipping MJ, Delalez NJ, Lim R, Berry RM, Armitage JP (2013) Load-Dependent Assembly of the Bacterial Flagellar Motor. *mBio* 4, e0055113
73. Fahrner KA, Ryu WS, Berg HC. (2003) Biomechanics: Bacterial flagellar switching under load. *Nature* 423:938-938
74. Inoue Y, Lo CJ, Fukuoaka H, Takahashi H, Sowa Y, Pilizota T, Wadhams GH, Homma M, Berry RM, Ishijima A. (2008) TorqueSpeed Relationships of Na⁺-driven Chimeric Flagellar Motors in *Escherichia coli*. *J. Mol. Biol.* 376(5): 1251-1259

75. Lo CJ (2007) Sodium energetics of chimeric flagellar motors in *Escherichia coli*. Ph.D. thesis. University of Oxford, Oxford, UK
76. Lackraj T, Kim JI, Tran SL, Barnett Foster DE (2016) Differential modulation of flagella expression in enterohaemorrhagic *Escherichia coli* O157:H7 by intestinal short-chain fatty acid mixes. *Microbiology* 162(10):1761-1772
77. Gauger EJ, Leatham MP, Mercado-Lubo R, Laux DC, Conway T, Cohen PS (2007) Role of motility and the *flhDC* Operon in *Escherichia coli* MG1655 colonization of the mouse intestine. *Infect Immun.* 75(7):3315-24
78. Tamar E, Koler M, Vaknin A (2016) The role of motility and chemotaxis in the bacterial colonization of protected surfaces. *Sci Rep.* 2016 6:19616
79. Blattner FR, Plunkett G 3rd, Bloch CA, Perna NT, Burland V, Riley M, Collado-Vides J, Glasner JD, Rode CK, Mayhew GF, Gregor J, Davis NW, Kirkpatrick HA, Goeden MA, Rose DJ, Mau B, Shao Y. (1997) The complete genome sequence of *Escherichia coli* K-12. *Science* 277(5331):1453-1462.
80. Barker CS, Pr BM, Matsumura P. (2004) Increased Motility of *Escherichia coli* by Insertion Sequence Element Integration into the Regulatory Region of the *flhD* Operon. *J. Bacteriol.* 186:7529-7537.
81. Stevenson K, McVey AF, Clark IBN, Swain PS, Pilizota T. (2016) General calibration of microbial growth in microplate readers. *Scientific Reports* 2016;6:38828
82. Pilizota T, Brown MT, Leake MC, Branch RW, Berry RM, Armitage JP. (2009) A molecular brake, not a clutch, stops the *Rhodobacter sphaeroides* flagellar motor. *Proc Natl Acad Sci USA.* 106(28):11582-11587
83. Martinez VA, Schwarz-Linek J, Reufer M, Wilson LG, Morozov AN, Poon WCK (2014) Flagellated bacterial motility in polymer solutions. *Proc Natl Acad Sci USA* 111(50):17771-17776









Supporting Information

Growth Media Osmolarities. Growth media osmolalities were measured with an osmometer (Micro-Digital Osmometer MOD200 Plus, Camlab, Cambridge, UK) and are given in Table S1.

Motility Media Viscosities. Motility media viscosities were measured with a rheometer (TA Instruments AR2000, cone-plate geometry, 60 cm, 0.5°) and are given in Table S2.

Supporting Figures. Supporting Figures to the main text are given with the captions.

Table 1. Media osmolalities

Media	Osmolality (mOsmol/kg)
VRB	92
VRB+40 mM sucrose	135
VRB+60 mM sucrose	157
VRB+100 mM sucrose	203
VRB+200 mM sucrose	320
VRB+400 mM sucrose	580
VRB+600 mM sucrose	877

Table 2. Measured media viscosities (in agreement with listed in [1])

Media	Viscosity (Pa s)
Motility Media	0.00112 ± 0.00001
Motility Media + 300 mM sucrose	0.00146 ± 0.00001
Motility Media + 600 mM sucrose	0.00192 ± 0.00002
Motility Media + 900 mM sucrose	0.00290 ± 0.00007
Motility Media + 1850 mM sucrose	0.0172 ± 0.0001

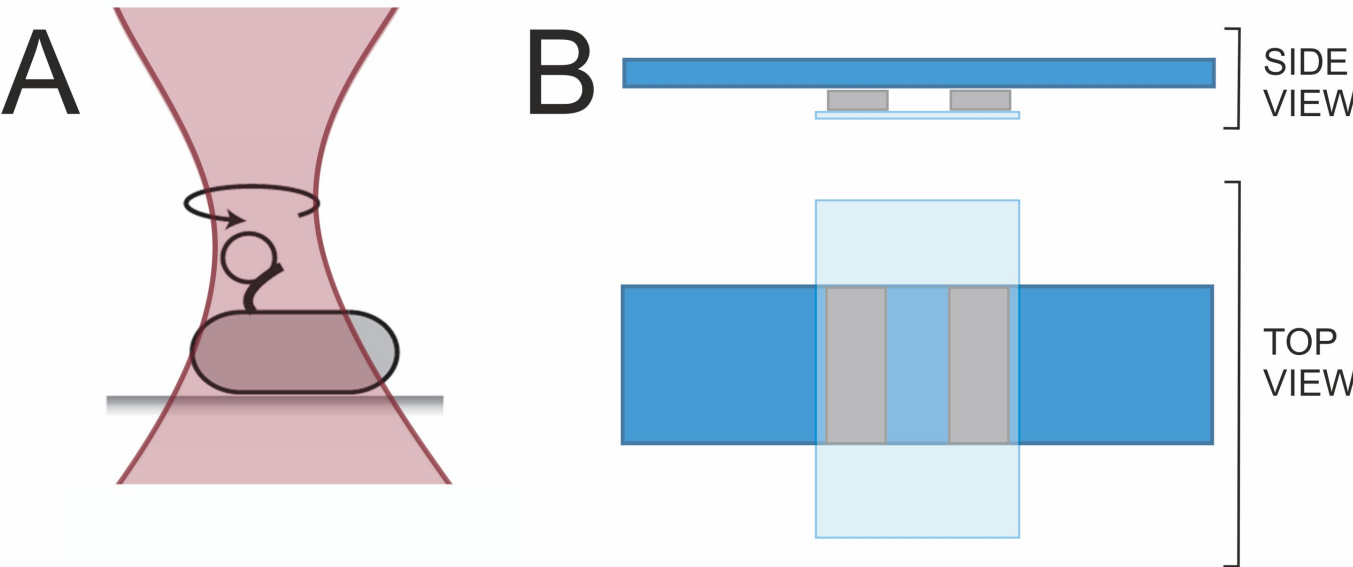


Fig. S 1. Schematic representation of the bead assay and tunnel slide used for measurements. (A) Genetically modified bacterial flagellar filament (FliC^{Sticky} [2]) stub was attached to a latex bead of 0.5 μm diameter. The bead was placed in a heavily attenuated optical trap and the bead rotation recorded via back focal plane interferometry (*Methods*). (B) A tunnel slide, formed by a double sided sticky tape separating a microscope slide and a glass cover slip, was used to deliver osmotic shocks. The slide was sealed with vaseline upon the osmotic shock to prevent evaporation.

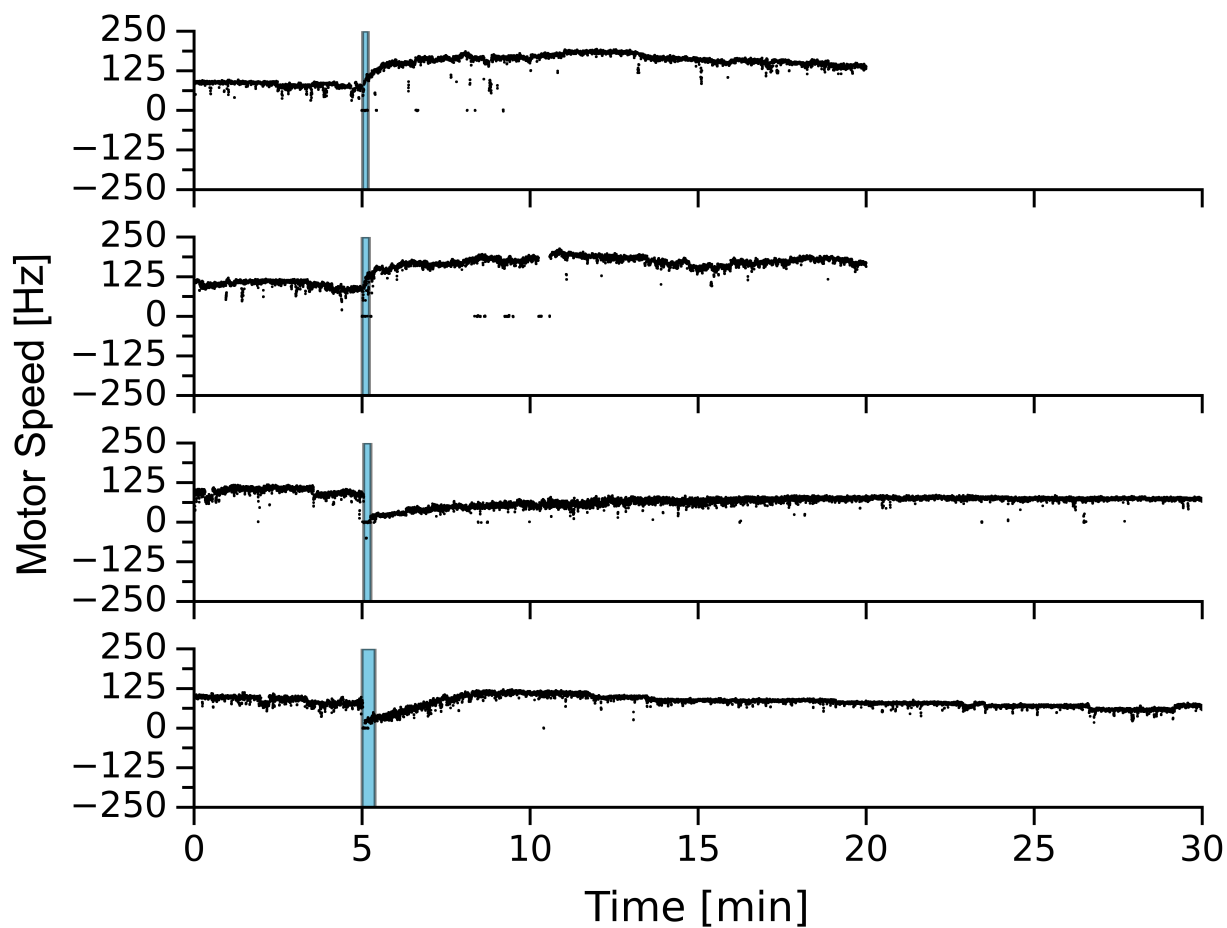


Fig. S 2. Four representative traces of motor speed against time for the ΔCheY strain KAF95. The blue shaded, vertical span marks the delivery of the osmotic shock. The top two traces have been recorded in the +111 mOsmol/kg condition, while the bottom two have been recorded in the +488 mOsmol/kg condition (base buffer is, as in all other experiments, VRB). We observe no switching before the shock, as expected from a ΔCheY strain that is smooth swimming, and also none after the shock. Yet, the speed dynamics are similar to KAF84 (Main text Fig. 3).

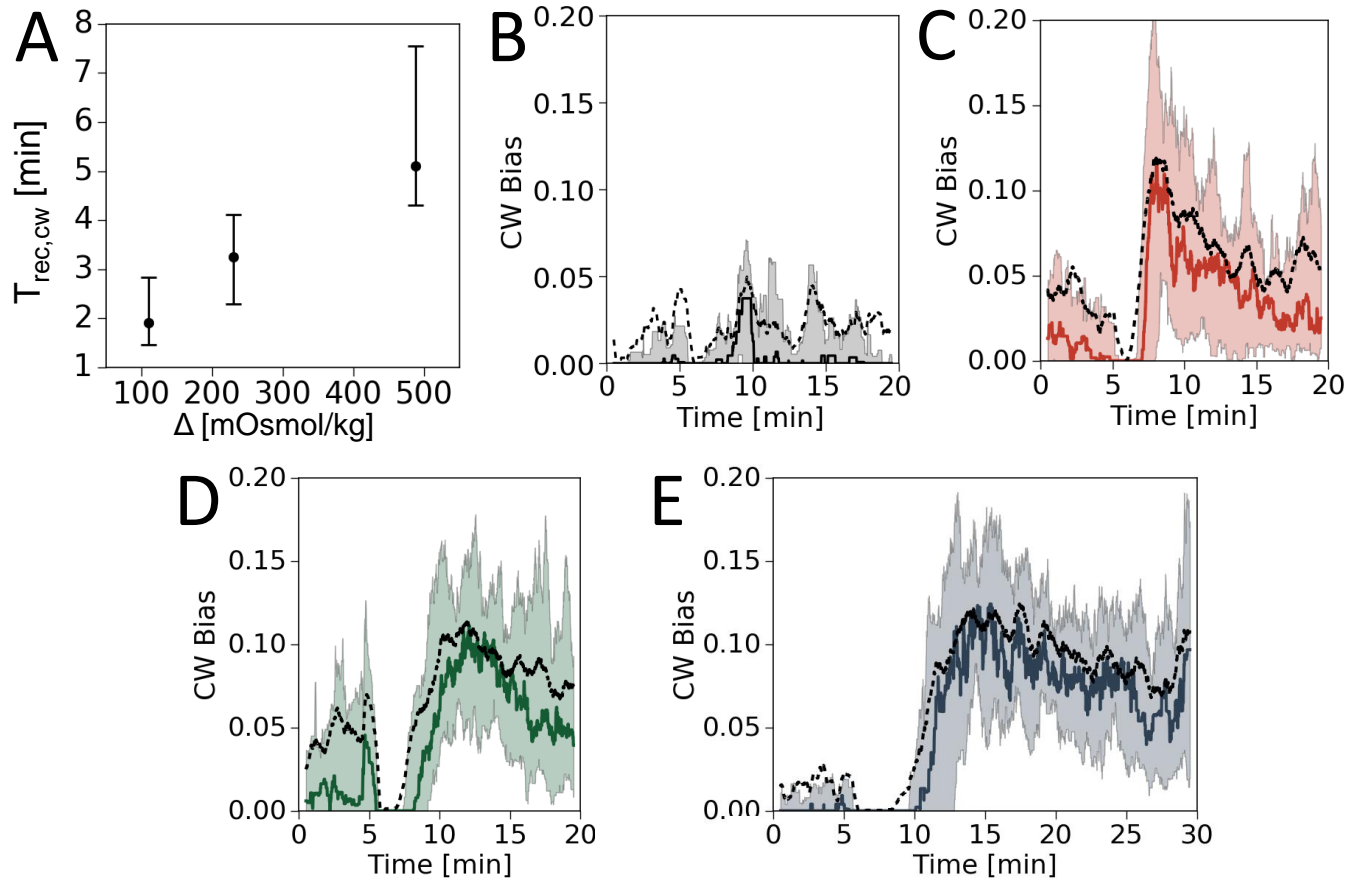


Fig. S 3. (A) Recovery Phase duration ($T_{rec,CW}$), calculated as the time needed for the post-shock median population bias to recover to the median VR Buffer bias (CW Bias=0.01, histogram in main text Fig. 2B). $T_{rec,CW}$ was calculated for each of the three shock conditions, whose biases are presented in panels C-D. The points represent times at which the post shock median reaches 0.01, relative to the time of shock delivery. The error bars give the populational variability in terms of recovery times for the 25th and the 75th percentile of population bias. (B) Buffer to buffer control flush CW Bias during the course of the experiment is given. Biases were calculated on a moving window of 60 s length and the VR Buffer was flown into the tunnel slide in the same way and duration as for the osmotic shock experiments. 12 cells in total are presented, the solid black line is the median, dashed is the mean and the shading represents the area between the 25th and 75th percentile. (C) Same as B but for the 111 mOsmol/kg osmotic upshift and the plot represents the median of the 22 single cell bias traces (thick red line), the mean (dashed black line) and the red shading is the area between the 25th and the 75th percentile. (D) and (E) are the same as C, only for the 230 mOsmol/kg (24 cells) and the 488 mOsmol/kg (23 cells) osmotic upshifts, respectively.

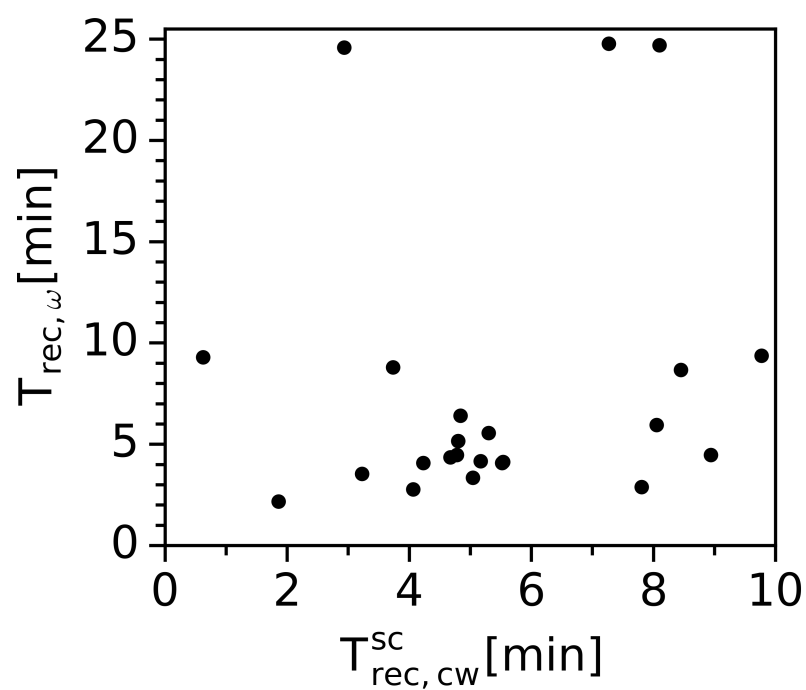


Fig. S 4. $T_{\text{rec}, \omega}$, the time necessary to recover the average value of single motor speed following an osmotic shock, is given against $T_{\text{rec}, \text{cw}}^{\text{sc}}$, the time between the administration of the shock and the first detected switch event (post shock). Values are plotted for every single cell in the +488 mOsmol/kg condition, showing that the recovery of speed and switching in individual motors do not occur simultaneously. +111 and +230 mOsmol/kg conditions show no correlation between the two; the speed recovery there is instantaneous or shorter than the switching recovery time.

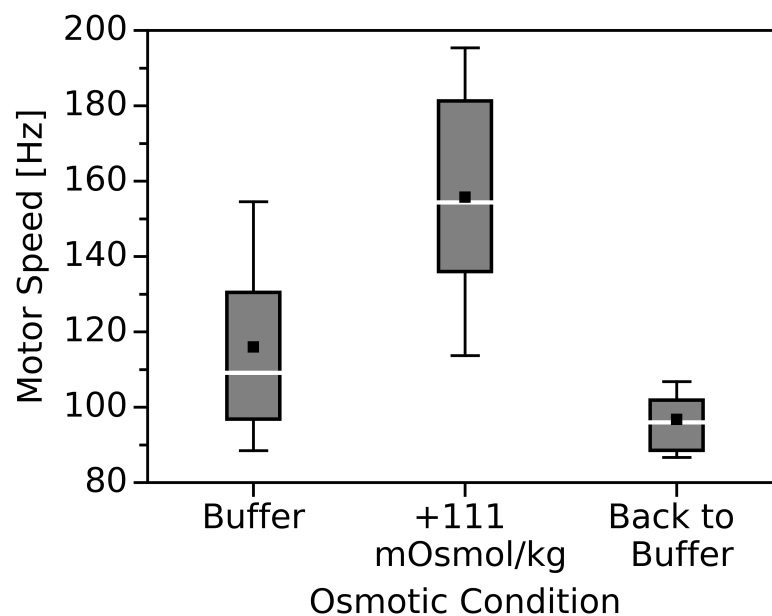


Fig. S 5. Osmolality induced speed increases are reversible. Box plot of motor speeds is shown against the final media cells are kept in. The box denotes the interquartile range and the whiskers the 10th and the 90th percentile. The Buffer (VRB) box contains the entire VRB speed distribution shown in SI Appendix Fig. S6. The 111 mOsmol/kg box contains speeds from osmotic upshock measurements 12 or more minutes after shock with 100 mM sucrose. The 'Back to Buffer' box contains measurements of motor speeds where cells were first exposed to 111 mOsmol/kg upshock in a tube, and after ~ 20 min recovery were transferred back to VRB. The measurements commenced ~ 20 min after return to VRB. Cells that have been washed back into VRB from VRB+111 mOsmol/kg have similar speed levels to the pre-shock VRB condition. The boxes contain 118, 45 and 27 cells respectively, with population average speeds of 116 ± 2 Hz, 156 ± 5 and 97 ± 2 Hz.

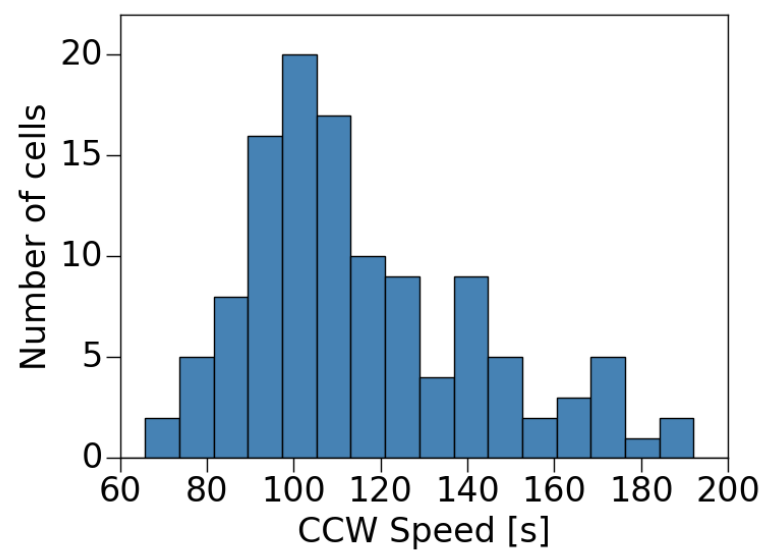


Fig. S 6. Histogram of single-motor speeds for *E. coli* KAF84 in the Volume Recovery Buffer (VRB). Each motor comes from a different single cell. Each speed is computed by taking the first 15 s of one of various recordings made in VRB, selecting the CCW speed from the trace and averaging it. The histogram contains 118 cells and the mean value of the distribution is 116 ± 2 Hz.

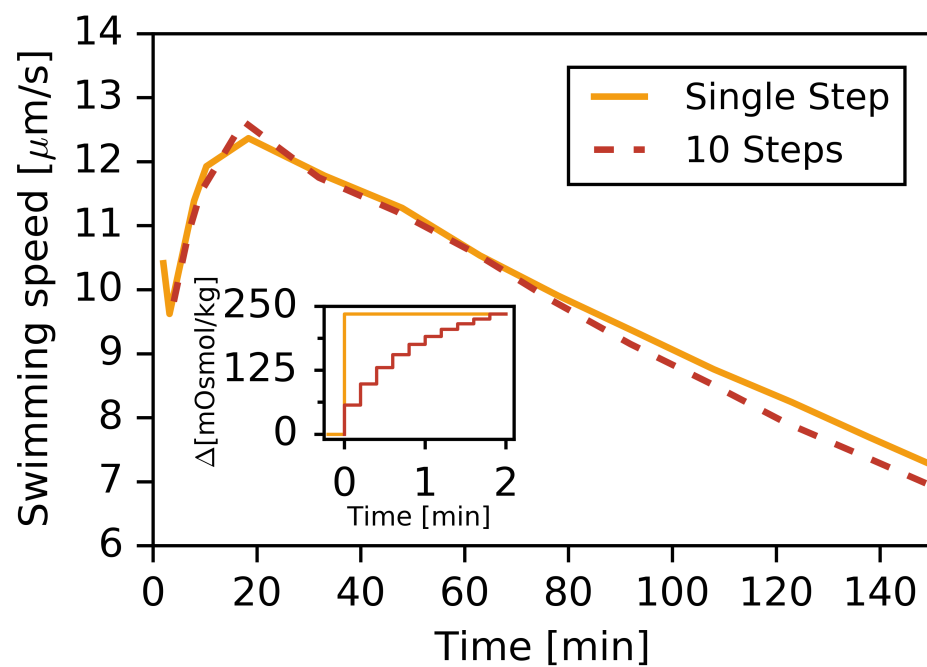


Fig. S 7. DDM measurement of swimming speeds of osmotically shocked cells, where the magnitude of the shock stays the same, but the shock is delivered over a different time interval. A single step bringing the cells up to 235 mOsmol/kg from VRB is given in orange. The same shock performed in 10 steps prior to DDM measurement is given in red (dashed line). The inset shows the change in osmolality cells experience over time with the two methods.

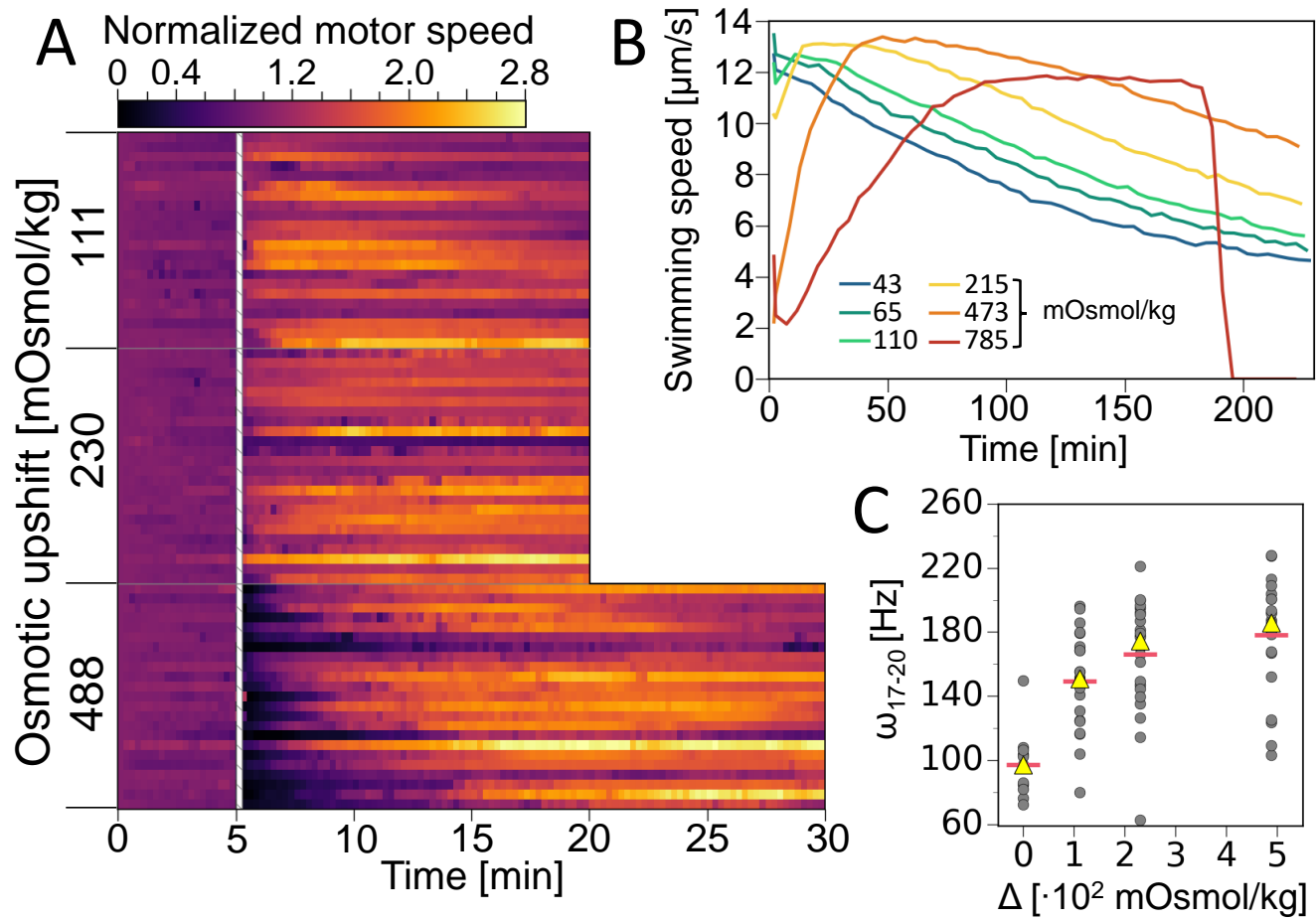


Fig. S 8. (A) Version of the main Fig. 3 where the motor and swimming speeds have been corrected for sucrose viscosity, under the assumption that no additional stators are incorporated at this increased load (see *Discussion* in the main text). Viscosity correction for 100, 200 and 400 mM sucrose used are a multiplicative factor of 1.057, 1.195 and 1.444, respectively (measured and listed in [1]). Each line represents a single motor speed trace binned into 15 s intervals where the color represents the height of the bin, normalized to the first bin. Results are grouped by upshock magnitude, as indicated on the left hand edge. The white hatched column represents the point where an osmotic shock was administered by exchanging VR Buffer for VR Buffer + sucrose and the flow lasted for 10-15 s. There are 22, 24 and 23 cells for the 111, 230 and 488 mOsmol/kg condition, respectively. The color map scale is given at the top of the figure. (B) DDM measurement of swimming speeds following an osmotic shock. Cells were shocked in microfuge tubes and brought into a microscope within 2 min. The legend shows shock magnitudes and the mean speed is the average of swimming speeds obtained for each time point in a range of different length scales (*Methods*). The systematic error of our measurements is then calculated as the standard deviation of the mean, and falls within $\sim 5\%$ of the mean value (here not plotted for clarity). The traces shown have been viscosity corrected as well, as free-swimming cells with the motor operating in linear-torque regime do not increase the swimming speeds with viscosities we used in our experiments [4]. (C) Viscosity corrected single motors speeds calculated as 3 min averages corresponding to a section between $t=17$ and $t=20$ min in A. The 0 mOsmol/kg condition is sampled from a set of buffer to buffer control flushes which were at least 20 minutes long (12 out of 18 control flushes). Red horizontal bars represent mean and yellow triangles median values.

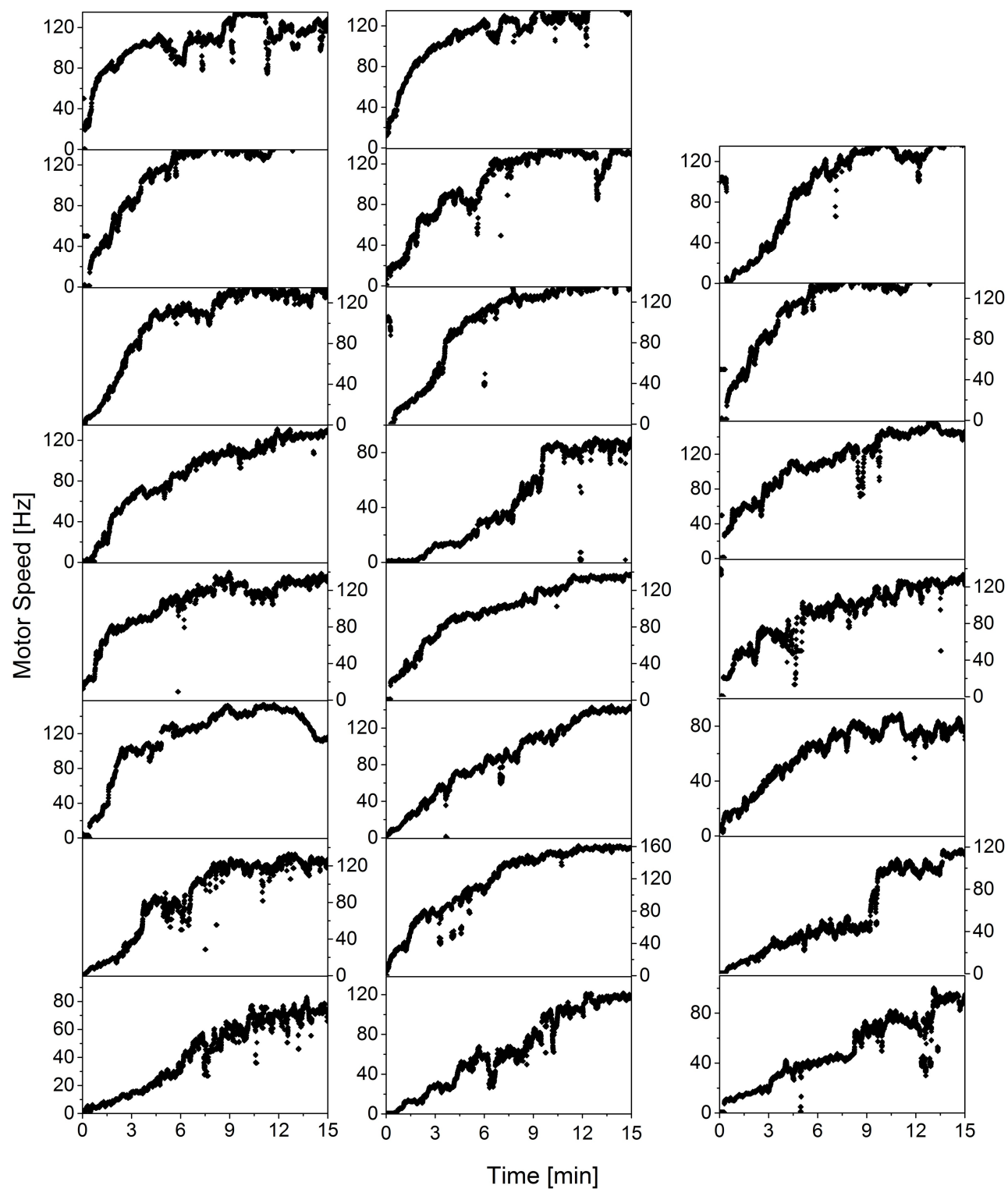


Fig. S 9. Traces of motor rotation after addition of 400 mM sucrose (all cells given in Fig. 2A and Fig. 3A of the main text are given). We do not plot the initial motor speed, and start at the point of speed drop due to an osmotic shock. Motor speeds were obtained as described in *Methods*.

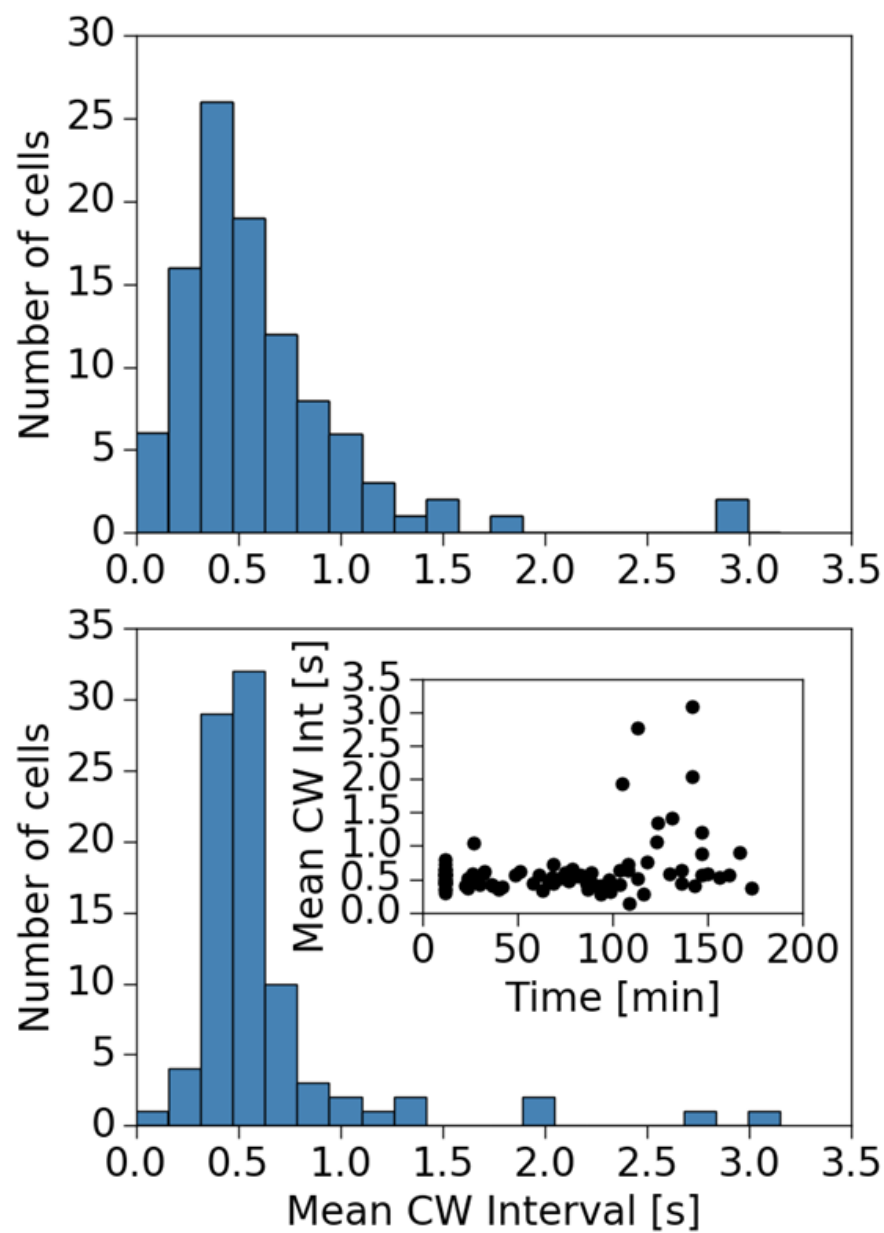


Fig. S 10. Top: Mean CW interval distribution ($\bar{\tau}_{CW}$) for cells in Volume Recovery Buffer. Motor rotation of 102 cells was sampled for 5 min and intervals counted as illustrated in SI Appendix Fig. S11. Bottom: Mean CW interval distribution for motors where the sampling interval (3 min) begins 12 or more minutes after an osmotic shock with 200 mM sucrose in VRB (+230 mOsmol/kg). The inset contains data from the histogram plotted against the start time of the sampling interval and $t=0$ corresponds to the osmotic shock.

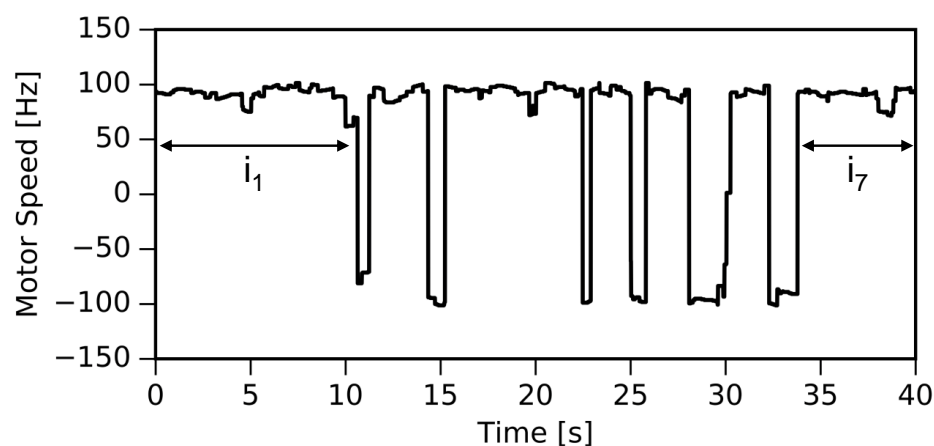


Fig. S 11. A portion of a single-motor speed trace illustrating the counting of interval lengths within a given sampling window. Positive speeds correspond to CCW rotation and negative to CW rotation. Intervals i_1 and i_7 are not included when calculating the mean CCW interval due to uncertainty in their beginning or end. Only intervals bounded by two CW intervals are counted. Similar holds true when calculating mean CW interval, only those bounded by two CCW intervals were included.

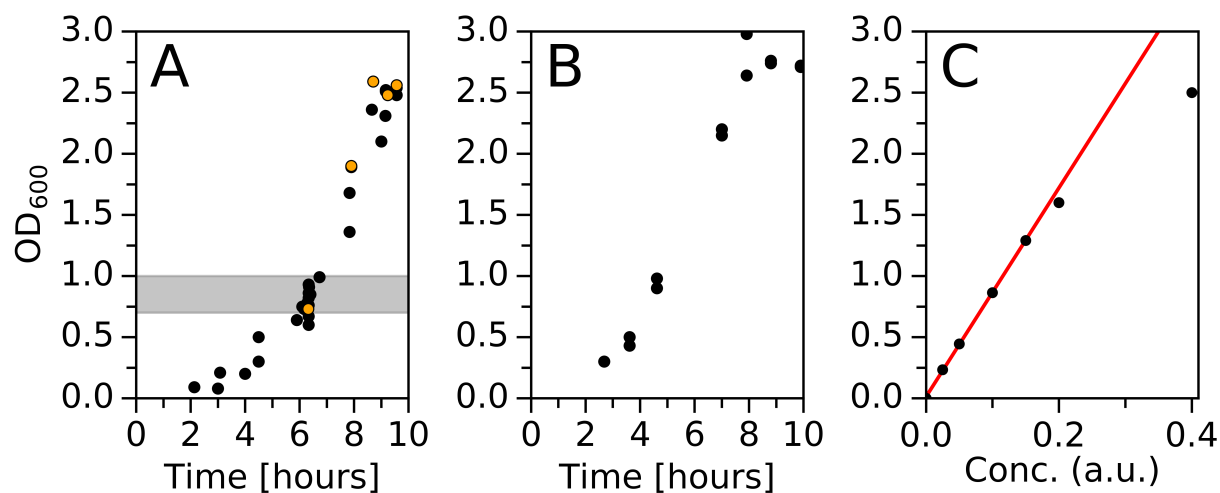


Fig. S 12. Growth curves of all strains used in this work are given in (A) and (B). (A) Optical density measured at 600 nm is given against time for growth of KAF84 (black) and KAF95 (orange) strain inoculated from an overnight frozen stock. (B) As in (A) but for MG1655 strain. (C) Calibration curve of our spectrophotometer. Various concentrations of cells were prepared to determine the range where OD is linear with the concentration. In (A) and (B) sample was diluted so that OD never surpassed 0.25 and ensuring we always measure within the linear range of our spectrophotometer. Points in (A) and (B) are taken from several different flasks, showing that growth from frozen samples is highly reproducible as all points collapse onto a single curve.

1. Swindells JF (1958) Viscosities of sucrose solutions at various temperatures: tables of recalculated values. United States, National Bureau of Standards
2. Fahrner KA (1995) Studies of bacterial flagellar motors and filaments. Ph.D. thesis. Harvard University, Cambridge, MA
3. Lo CJ (2007) Sodium energetics of chimeric flagellar motors in *Escherichia Coli*. Ph.D. thesis. University of Oxford, Oxford, UK
4. Martinez VA, Schwarz-Linek J, Reufer M, Wilson LG, Morozov AN, Poon WCK (2014) Flagellated bacterial motility in polymer solutions. *Proc Natl Acad Sci USA* 111(50):17771-17776